

# UC San Diego

## UC San Diego Previously Published Works

**Title**

Holocene Paleointensity of the Island of Hawai`i From Glassy Volcanics

**Permalink**

<https://escholarship.org/uc/item/22d255g5>

**Journal**

Geochemistry Geophysics Geosystems, 19(9)

**ISSN**

1525-2027

**Authors**

Cromwell, G  
Trusdell, F  
Tauxe, L  
et al.

**Publication Date**

2018-09-01

**DOI**

10.1002/2017gc006927

Peer reviewed

# Holocene paleointensity of the Island of Hawai'i from glassy volcanics

G. Cromwell,<sup>1,2</sup> F. Trusdell,<sup>3</sup> L. Tauxe,<sup>2</sup> H. Staudigel,<sup>4</sup> and H. Ron<sup>5</sup>

G. Cromwell, California Water Science Center, United States Geological Survey, 4165 Spruance Rd  
Suite 200, San Diego, CA, 92101-0812, USA

H. Ron, Hebrew University of Jerusalem, Jerusalem, Israel

H. Staudigel, Institute of Geophysics and Planetary Physics, Scripps Institution of Oceanography,  
University of California San Diego, 9500 Gilman Dr, La Jolla, CA, 92093-0225, USA

L. Tauxe, Geosciences Research Division, Scripps Institution of Oceanography, University of California San Diego, 9500 Gilman Dr, La Jolla, CA, 92093-0220, USA

F. Trusdell, Hawaiian Volcano Observatory, United States Geological Survey, Hawaii, 96718, USA

<sup>1</sup>California Water Science Center, United

This article has been accepted for publication and undergone full peer review but has not been through the copyediting, typesetting, pagination and proofreading process which may lead to differences between this version and the Version of Record. Please cite this article as  
doi: 10.1002/2017GC006927

© 2017 American Geophysical Union

Received: Mar 21, 2017; Revised: Aug 10, 2017; Accepted: Sep 05, 2017

**Abstract.** This study presents new high-quality paleointensity records and  $^{14}\text{C}$  radiocarbon age determinations from the Island of Hawai‘i during the Holocene. Previous studies on Hawai‘i use experimental methods and statistical selection criteria that may produce inaccurate geomagnetic field strength estimates. Additional high-quality paleointensity results can be used to evaluate the existing Hawaiian dataset and investigate Holocene geomagnetic field behavior. New paleointensity sites from 22 lava flows were calculated using the IZZI-Thellier laboratory technique and a strict set of selection criteria. Rapidly cooled, glassy volcanic material was collected for all sites. Isotopic age determinations range from

---

States Geological Survey, California, USA

<sup>2</sup>Geosciences Research Division, Scripps  
Institution of Oceanography, University of  
California San Diego, California, USA

<sup>3</sup>Hawaiian Volcano Observatory, United  
States Geological Survey, Hawaii, USA

<sup>4</sup>Institute of Geophysics and Planetary  
Physics, Scripps Institution of Oceanography,  
University of California San Diego, California,  
USA

<sup>5</sup>Institute of Earth Science, Hebrew  
University of Jerusalem, Jerusalem, Israel

270- > 10,000 years before present (nine new  $^{14}\text{C}$  ages are also presented as part of this study). The median intensity for the 22 flows is  $47.5 \mu\text{T}$ , with a median absolute deviation uncertainty of  $5.6 \mu\text{T}$ ; substantially greater than the present day field strength at Hawai'i ( $\sim 36 \mu\text{T}$ ). These new results are comparable to previously published data from this location and are consistent with global paleointensity models. There is no evidence of an intensity "spike" at 3,000 years before present, as seen in the Levant and elsewhere. Previously published data vary in intensity by experimental technique relative to data using glassy material and strict selection criteria. Non-Thellier-type data are biased low, a result of these techniques estimating intensity from possibly non-single domain magnetic carriers. Thellier-Thellier data are biased high, the reasons for which remain unclear as no cooling rate effect was demonstrated and we were unable to reproduce the high bias with different selection criteria.



## 1. Introduction

Global geomagnetic field models use paleomagnetic data to predict magnetic field directions and intensity at any point on the Earth's surface. Of particular interest to researchers is the behavior of the geomagnetic field over the last ten thousand years (Holocene). High resolution paleomagnetic data from archaeomagnetic, volcanic and sedimentary records allows for the development of detailed global geomagnetic field models for the Holocene (e.g., *Nilsson et al.* [2014]; *Pavón-Carrasco et al.* [2014]; *Constable et al.* [2016]). These models predict variations in paleodirection and paleointensity and allow researchers to evaluate regional and global behaviors of the recent geomagnetic field. Essential to this modeling effort is the acquisition of high quality directional and intensity data from new study areas, especially those from outside of Europe and the Middle East where the vast majority of data come from presently. Also important is the reevaluation of existing data to ensure that these models incorporate accurate measurements of the magnetic field.

The Island of Hawai'i (Figure 1) is a well studied location for paleomagnetic studies of Holocene aged rocks. The island features three active volcanoes, one of which, Kīlauea, has been continuously erupting since 1983. Surficial lava flows on the island range in age from present day at Kīlauea to 250,000-700,000 years before present (yr B.P.) in the Kohala section [*Wright et al.*, 1992]. Lava flow ages are constrained by historic records and  $^{14}\text{C}$  isotopic dating on flows older than a few hundred years before present (e.g., *Lockwood* [1995]).

A number of studies have targeted modern, historic and ancient lavas on Hawai'i for paleodirectional and paleointensity analysis with a focus on understanding the behavior of the Earth's magnetic field (e.g., *Coe et al.* [1978]; *Pressling et al.* [2006]; *de Groot et al.* [2013]). In par-

allel with these efforts, there has been a focus on using historic lava flows to test the efficacy of paleointensity laboratory methods. The benefit of conducting paleomagnetic experiments on modern lava flows is that the experimental results can be compared to known values of the Earth's magnetic field: the 1960 Kīlauea eruption is one such test site. At least 13 different studies have tested a variety of paleointensity methods on the 1960 Kīlauea flow (see *Cromwell et al.* [2015a]).

The accuracy and precision of estimates of geomagnetic intensity vary depending on the methodology and quality of paleointensity data included in the calculations. Paleointensity results from the 13 studies conducted on the 1960 lava flow show a high degree of variability (e.g., *Love and Constable* [2003]; *Herrero-Bervera and Valet* [2009]; *Cromwell et al.* [2015a]), with individual specimen estimates ranging from  $\sim 60\%$  to  $> 200\%$  of the expected field strength ( $36.1 \mu\text{T}$ ). Bootstrapped calculations of field strength show that estimates of mean and median intensity are within error of the expected value, but are likely to slightly overestimate the field [*Cromwell et al.*, 2015a] and the entire data set is an order of magnitude larger than ordinary paleointensity studies which typically have fewer than ten specimens. It is unclear whether the variability observed in the 1960 flow is typical of published results from other lava flows, although *Tauxe et al.* [2013] and *Cromwell et al.* [2015b] suggest that the existing database of ancient field intensities may be biased high. In contrast, *Cromwell et al.* [2015a] show that paleointensity experiments conducted on glassy or very fine grained lava flow tops, combined with strict selection criteria, can yield results that are accurate to within  $3 \mu\text{T}$  of the expected magnetic field strength. Moreover, the results in *Cromwell et al.* [2015a] do not exhibit any propensity towards overestimating the expected intensity field value.

In this study we present an expanded set of high quality paleointensity results, with new  $^{14}\text{C}$  isotopic ages, from lava flows emplaced on Hawai‘i during the Holocene. We employ the sampling strategy and experimental methodology of *Cromwell et al.* [2015a] and compare our results to other paleointensity studies conducted on the island. We further evaluate our findings in the global context of the Holocene geomagnetic field and test whether we observe an exceptionally high “spike” in field intensities at about 3,000 yr B.P., as is seen in the Levant [Ben-Yosef *et al.*, 2009; Shaar *et al.*, 2011, 2016].

## 2. Sample Collection

We collected unoriented hand samples of glassy volcanic material from 70 sampling sites, representing 60 Holocene lava flows (270– > 10000 yr B.P.) on the Island of Hawai‘i (Table 1). Site selection was guided by availability of age information and outcrop accessibility. Samples were taken from rapidly cooled portions of each lava flow, generally from the upper 1–2 cm of pāhoehoe flow tops (Figure 2a), aa spires (Figure 2b), and other exposed flow surfaces (Figure 2c). Subaerial volcanic glass forms when upper portions of a lava flow cool after contacting the surrounding air. As a result, volcanic glass is readily found on the tops of recently emplaced lava flows. Chemical and physical weathering, and erosional processes, remove this glassy material, and over time the presence of volcanic glass of lava flow tops is reduced. We observed this trend in our sample collection efforts on Hawai‘i, where younger lava flows (less than a few thousand years old) generally contained characteristic glassy flow tops, while older lava flows were more likely to lack glassy material. We collected glassy bits when present, and where none were present we sampled the most fine-grained material possible.

In the laboratory we subsampled the rocks collected from each site, preferentially selecting the most glassy, or fine-grained crystalline material, with a minimum magnetic moment of  $10^{-10}$

Am<sup>2</sup>. Specimens that were exceptionally dirty or exhibited signs of alteration were submerged in an ultrasonic bath for 15 minutes, in a dilute 10% HCl solution, to remove any dirt or alteration materials that could acquire a partial thermal remanent magnetization (pTRM) during laboratory heating steps. The ultrasonic bath was chilled to 30°C to prevent any additional pTRM acquisition.

### 3. <sup>14</sup>C isotopic Dating

Radiocarbon is obtained from charcoal excavated from under flow margins, associated with overlying flow. Most charcoal is formed from leaves, stems, small twigs, and roots, which minimizes the chance of contamination by “old wood”. *Lockwood and Lipman* [1980] present guidelines for the recovery of charcoal beneath young basaltic lava flows.

All but six of our 70 sites have associated <sup>14</sup>C ages (see Table 1). Nine new <sup>14</sup>C ages are presented as part of this study (Table 2). Twenty-four sites were dated by *Lockwood* [1995] (Table 3), 15 sites by *Trusdell et al.* [2006] (Table 4), and 15 sites were dated by *Trusdell and Lockwood* [2017] and *Trusdell and Lockwood* [in press] (Table 5). Ages for the six sites without published <sup>14</sup>C dates (hw107, hw122, hw131, hw219, hw230, and hw235) are estimated from the digital database of the geologic map of the Island of Hawai‘i [*Trusdell et al.*, 2006].

Many of the results in Table 2 are conventional ages determined at the United States Geological Survey (USGS) laboratory in Reston, Virginia. In addition, accelerator mass spectrometer (AMS) ages were made at USGS and other laboratories. For samples recovered at multiple locations from under the same lava flow, we weight each age by the inverse of its variance to yield a mean age [*Taylor*, 1997].

Charcoal was the only material dated and was hand picked from field samples dried for several hours at low temperature. Samples selected for dating were converted to pure carbon, in the

form of graphite, at the USGS Radiocarbon Laboratory in Reston, Virginia. Radiocarbon dating was done by AMS at the Center for Accelerator Mass Spectrometry at Lawrence Livermore National Laboratory in Livermore, California, the NSF-Arizona AMS facility at the University of Arizona in Tucson, Arizona, or the SUERC, NERC radiocarbon laboratory in Kilbride, Scotland, United Kingdom. Contaminant carbon was removed from raw sample material using successive acid and alkali washes: 1 M HCl (60°C for two hours), followed by 0.1 M NaOH (60°C overnight), and a final wash at 1 M HCl (60°C for two hours). Neutralized samples were placed in a 50°C oven until dry. Each sample was then placed in a sealed, air-free 6 mm Vycor tube with CuO, and combusted at 900°C to produce CO<sub>2</sub>. The CO<sub>2</sub> was cryogenically isolated from volatile gases and H<sub>2</sub>O in a high-vacuum manifold. Finally, each CO<sub>2</sub> sample was reduced to 1 mg carbon as graphite precipitated on 63 mesh Fe powder in the presence of hydrogen at 575°C [Vogel *et al.*, 1984]. The resultant graphite was then pressed into an aluminum target and sent to one of the AMS labs for dating. Radiocarbon ages were determined using an assumed  $\delta^{13}\text{C}$  of -25 ppm with a Libby half-life of 5,568 years. Radiocarbon ages in Table 2 are reported with  $1\sigma$  uncertainty. All ages were calibrated to calendar years using the CALIB 6.0 Radiocarbon Calibration Program [Stuiver *et al.*, 1998a, b] in conjunction with the IntCal04 calibration datasets [Reimer *et al.*, 2004]. The calibrated age ranges in Table 2 encompass all possible calendar years for a given radiocarbon age at two standard deviations; however, all ages shown in the table are radiocarbon years before present.

#### 4. Paleointensity Experiment

All paleomagnetic experiments were conducted in the paleomagnetism laboratory at Scripps Institution of Oceanography at the University of California San Diego. The IZZI-modified double heating paleointensity method was used on all specimens [Tauxe and Staudigel, 2004]

and a laboratory field of 20  $\mu$ T was applied during in-field heating treatments. Thermal heatings were conducted in custom-built ovens, and magnetic measurements were performed in a 2G Cryogenic Magnetometer. The IZZI experiment was carried out on each specimen until at least 95% of the natural remanent magnetization (NRM) was removed or until the specimen showed significant signs of alteration and were expected to fail our selection criteria.

The IZZI experiment consists of a series of double-heating steps whereby the specimen is cooled either in the laboratory field or in zero-field. The order of the cooling steps alternates between in-field cooling followed by zero-field (IZ) and zero-field cooling followed by in-field (ZI) at successively higher temperatures until the entire natural remanence (NRM) has been replaced by a laboratory acquired thermal remanence (TRM). At every other temperature step, a lower temperature step is repeated, providing a check if the capacity of the specimen to acquire a pTRM changed during heating.

#### 4.1. Selection Criteria

The Thellier GUI Auto Interpreter [Shaar and Tauxe, 2013] was used to analyze all experimental results (the Auto Interpreter can be downloaded as part of the *PmagPy* software distribution [Tauxe *et al.*, 2016] at <https://earthref.org/PmagPy/>). For our data interpretation, we use the selection requirements (see Table 6) implemented by recent paleointensity studies on rapidly cooled volcanic material [Cromwell *et al.*, 2015a, b]. The statistical limits listed in Table 6 ensure that accepted specimens contain only a single directional magnetic component and have near-linear slopes in their NRM/TRM Arai plots [Nagata *et al.*, 1963]. This set of selection criteria was referred to as “CCRIT” by Tauxe *et al.* [2016].

We briefly describe the CCRIT selection statistics, and refer the reader to Paterson *et al.* [2014] for a detailed discussion of all paleointensity statistics used in this study and in other

publications. *SCAT* is a boolean statistic (with a threshold value of  $\beta=0.1$ ) that calculates the degree of scatter about a best-fit slope over the range of NRM/TRM temperature steps used to calculate the paleointensity value [Shaar and Tauxe, 2013]. A specimen passes the *SCAT* criterion if all points associated with the chosen temperature range fall within the *SCAT* polygon (shown as dashed gray lines in Figure 4). *FRAC* uses a vector difference sum calculation to determine the fraction of NRM used to calculate a paleointensity value [Shaar and Tauxe, 2013]. *Gap Max* is the maximum difference between two NRM/TRM steps in the selected temperature range [Shaar and Tauxe, 2013].  $\beta$  is a measure of the relative variance about the best-fit line between selected NRM/TRM temperature steps, and is defined as the ratio of the standard error of the slope to the absolute value of the slope [Coe et al., 1978; Tauxe and Staudigel, 2004]. *DANG* (Deviation ANGLE) is the angle between the NRM steps of the best-fit line and the angle of a line that anchors the center of mass to the origin [Tauxe and Staudigel, 2004].  $MAD_{free}$  (maximum angle of deviation) is the scatter about the best-fit line of the NRM components in an Arai plot [Kirschvink, 1980].  $\vec{k}'$  is a measure of the curvature of data points in an Arai plot over a select temperature range [Paterson et al., 2014].

## 5. Paleointensity Results

A total of 123 specimens from 25 out of 70 sampled sites (22 lava flows) meet all selection requirements. Sites hw100 and hw211, hw118 and hw120, and hw121 and hw234 are from the same lava flow; successful specimens from each lava flow are combined and tested to ensure that the combined specimens pass all site level requirements. We refer to these combined sites as hw100, hw118, and hw121 from here on. Estimated paleointensity results from all accepted sites are listed in Table 7, and plotted as red squares in Figure 3. Specimen-level intensity estimates, statistics, and experimental measurements are in the MagIC database at

<https://earthref.org/MagIC/DOI/XXXXX>. Successful sites range in age from 270 to 6500 yr B.P., and have a median paleointensity value of  $47.5 \mu\text{T}$  with a median absolute deviation uncertainty of  $5.6 \mu\text{T}$ .

Representative specimen results from the IZZI paleointensity experiment are shown in Figure 4. Examples of two successful specimens from site hw103 (Figure 4a and b) show some of the within-site variability of accepted specimens. Specimen hw103c4 (Figure 4a) has a linear slope through the entire NRM/TRM diagram, with a single magnetic component (see inset Zijdeveld diagram) and no signs of alteration. Specimen hw103b1 (Figure 4b) also has a single directional component, but shows signs of thermal alteration beginning at about  $350^{\circ}\text{C}$ , as evident by scattered pTRM checks. Although there is evidence for some alteration, hw103b1 passes our selection criteria because the low-temperature component in the Arai plot is linear and accounts for more than 78% of the NRM fraction. The difference in estimated paleointensity between these specimens hw103c4 and hw103b1 is less than  $1 \mu\text{T}$ . Figure 4c and Figure 4d show two specimens from site hw118: hw120a3 and hw120a4. Specimen hw120a3 (Figure 4c) is a very well-behaved specimen that has a linear Arai plot and passes all selection requirements. Specimen hw120a4, obtained from the same lava flow, however, fails the  $\vec{k}'$  criterion across all acceptable NRM fractions (as determined by *FRAC*) and is rejected from further analysis. It is worth noting that some thermal alteration effects may be undetectable using standard pTRM checks (e.g., Coe [1967]; Coe *et al.* [1978]; Wang and Kent [2013]; Zhao *et al.* [2014]); in specimen hw120a3 for example, the small “kink” in the Arai plot at  $\sim 450^{\circ}$  could be the result of magnetochemical changes [Mankinen and Champion, 1993], evident by the slight pTRM check offset at  $400^{\circ}$ . Although alteration may occur in cases like this, the continuing temperature steps do not deviate substantially from the least-squares line and paleointensity estimates



through these temperature steps should not be affected so long as appropriate selection criteria are in place. The strict CCRIT requirements flag any heating steps or pTRM checks that are significantly altered or otherwise deviate from the best-fit line, which should ensure consistent within-site paleointensity estimates.

Curved Arai plots without obvious signs of alteration are indicative of pseudo-single-domain or multi-domain behavior, or these concave-up diagrams could also be the result of undetectable thermal alteration effects. Regardless of the causal mechanism, curved Arai plots should be considered unreliable recorders of paleointensity because they present subjective intensity interpretations that are often inconsistent between specimens from the same site. As pointed out by *Cromwell et al.* [2013], even fields calculated from total TRMs tend to be significantly lower than those from straight Arai plots. That is certainly the case in this example, as normalizing the remanence by total TRM (shown as the green line) of specimen hw120a4 gives an ancient field estimate of  $35.7 \mu\text{T}$ , compared to  $51.3 \mu\text{T}$  estimated from the eight specimens in hw118 that passed our criteria (including specimen hw120a3). It is possible that this specimen has suffered from the aging phenomenon documented by *Shaar and Tauxe* [2015] whereby even pseudo-single domain remanences are found to be unstable over as little as two years. If hw120a4 is indeed multi-domain, one alternative could be to apply the correction technique of *Wang and Kent* [2013] and compare that result to other specimens in the site. Such a correction could, in principle, provide additional results. However, given the substantial doubt cast on the stability of pseudo-single domain remanences, combined with the proven reliability of the approach taken in this study, we have not attempted the *Wang and Kent* [2013] method here.

While many of our paleointensity results in Figure 3 approximate the CALS10k.2, HFM.OL1.A1 [*Constable et al.*, 2016] and PFM9K global paleointensity model [*Nilsson et al.*,

2014] curves, most sites have higher than predicted intensity values. Nine of our sites agree with one or more of the global models, within  $1\text{-}\sigma$  uncertainty, while 11 sites are higher and two sites are lower than the model predictions. The median value of our results ( $47.5\text{ }\mu\text{T}$ ) is higher than the present day field strength at the Island of Hawai‘i ( $\sim 35\text{ }\mu\text{T}$ ), consistent with previously published data from Hawai‘i (see Discussion section). According to our results, geomagnetic field strength at Hawai‘i reached a maximum average value of  $\sim 67\text{ }\mu\text{T}$  at around 1800 yr B.P., and a minimum value of  $35\text{ }\mu\text{T}$  at around 2000 yr B.P.; suggesting that large variations in field strength may occur on decadal and centennial timescales, similar to what is observed in other regions (e.g., *Shaar et al.* [2011, 2016]).

The maximum intensity value we observe ( $67\text{ }\mu\text{T}$ ) at two sites with ages of 1,647 and 1,838 yr B.P. (hw229 and hw208, respectively; see Table 7) has an equivalent virtual axial dipole moment (VADM) of  $150\text{ ZAm}^2$ , about twice the strength of the present day field,  $\sim 80\text{ ZAm}^2$ . This maximum value is somewhat lower and temporally inconsistent with the geomagnetic “spike” (defined as  $\text{VADM} > 160\text{ ZAm}^2$ , or  $\sim 71\text{ }\mu\text{T}$  at the latitude of Hawai‘i), observed in the Levant at  $\sim 3000\text{ yr B.P.}$  [*Ben-Yosef et al.*, 2009; *Shaar et al.*, 2011, 2016]. As seen in Figure 3, sites with ages similar to the Levant “spike” have intensities that range from about  $40$  to  $60\text{ }\mu\text{T}$ . The only successful site from this study emplaced at 3000 yr B.P. (hw134) has a paleointensity value of  $41.7\text{ }\mu\text{T}$ , with an equivalent VADM of  $93.2\text{ ZAm}^2$ ; slightly greater than the present day field intensity. We recovered reliable paleointensity results from most sampled sites with ages  $\sim 3000\text{ yr B.P.}$ , indicating that there is no contemporaneous “spike” between Hawai‘i and the Levant, at least from this dataset.

## 6. Discussion

In this section we evaluate the results in this study relative to other similarly aged Holocene intensity data from the Island of Hawai‘i. Of special interest is the variation of geomagnetic field intensity over the last few thousand years, and the behavior of our strict experimental and statistical methodology compared to other paleointensity studies. For comparison, we include all published paleointensity data from Hawai‘i with at least three accepted specimens per site, and volcanic flow ages less than 6,000 yr B.P. A total of 138 paleointensity sites from 20 studies were downloaded from the online MagIC (<https://earthref.org/MagIC>; *Tauxe et al.* [2016]) and Geomagia (<http://geomagia.gfz-potsdam.de>; *Brown et al.* [2015]) paleomagnetic databases. These published data are also shown in Figure 3 and are coded by reference and experimental type. For this discussion, the modern and historical paleointensity results of *Cromwell et al.* [2015a] will be considered as part of our new data from the Island of Hawai‘i because those results were derived using the same experimental and analytical procedures.

*Tauxe and Yamazaki* [2015] reviewed the basic paleointensity methods in common use. Here we provide a brief introduction to the increasingly complicated experimental protocols used to produce the field estimates in Figure 3. The classic Königsberger-Thellier-Thellier [*Thellier and Thellier*, 1959] is a double heating method whereby both heating steps to a given temperature are performed in-field (here termed II). The modification by Coe is a double heating method whereby the first heating step is performed in zero-field and the second is in in-field (ZI) [*Coe*, 1967]. A similar method proposed by *Aitken et al.* [1988] switches the order of the steps to in-field first followed by the zero-field step (IZ). As already noted, the IZZI method [*Yu et al.*, 2004; *Tauxe and Staudigel*, 2004], alternates between IZ and ZI on consecutive heating steps. In all of these “Thellier-type” protocols, checks can be applied as a test for alteration, and

lower temperature infield heating steps can be repeated to test whether the remanence carrying capacity of the specimen has changed. Moreover, the linearity of the NRM remaining against pTRM gained plots (so-called Arai plots) allows a partitioning of behaviors into ‘straight-line’ or ‘curved’ based on the  $\vec{k}'$  criterion which *Paterson* [2011] ascribes to single-domain like and multi-domain like remanence carriers the latter of which frequently fails the ‘reciprocity’ condition mandated by *Thellier and Thellier* [1959].

In addition to double heating (Thellier-type) methods the published data sets include other types of intensity methods (pseudo-Thellier, microwave, multi-specimen, Shaw, etc.). The pseudo-thellier method (PT) developed by *Tauxe et al.* [1995] was originally intended as a method to estimate relative paleointensity in sediments, but was applied to igneous rocks by *de Groot et al.* [2013] who “calibrated” the relative paleointensities using results obtained from historical lava flows. The “microwave” method (MW) of e.g., *Walton et al.* [1992] strives to heat only the magnetic particles through microwave stimulation, leaving the matrix cool, thereby reducing thermal alteration. “Multi-specimen” techniques reduce the number of heating steps performed on each specimen by heating different specimens to a target temperature (assumed to be below the onset of alteration) and cooling them in different laboratory fields. The particular protocol used in the Hawaiian database is that of *Dekkers and Böhnel* [2006] as modified by *Fabian and Leonhardt* [2010] and is here referred to as the ‘MSP-DSC’. The so-called “Shaw” method (S), developed by *Shaw* [1974] comprises first a complete demagnetization of the specimen using alternating fields (AF) followed by giving the specimen a total anhysteretic remanence (ARM) and AF demagnetizing that applied remanence. The specimen is then given a total TRM which is AF demagnetized and finally a second ARM followed by AF demagneti-

zation. Detection of alteration is performed by comparing the coercivity spectra of the ARMs before and after heating. Paleointensity data from all other methods are also plotted in Figure 3.

The distribution of published intensity data in Figure 3 is similar to that of our data and that of *Cromwell et al.* [2015a]. Intensity estimates for the last few hundred years cluster along the global paleointensity model curves, but tend to be more variable farther back in time and may tend to overestimate the predicted field strength of the global models. At first glance, it seems that the Thellier-type data are in general higher than the non-Thellier type data, with our data splitting the difference.

In order to delve deeper into the published data from Hawai‘i, we plot several subsets of the Hawai‘i data set as cumulative distribution function (CDF) diagrams in Figure 5. In Figure 5a we plot all Hawai‘i paleointensity data (including results from this study), our data and those of *Cromwell et al.* [2015a], and published data separated by experimental type: Thellier-type (Thellier-, Coe-, Aitken-, and IZZI-Thellier) versus non-Thellier data (pseudo-Thellier, microwave, MSP-DSC, and Shaw). Figure 5b and c subdivides Thellier-type and non-Thellier-type data by specific technique.

Paleointensity estimates for this study and *Cromwell et al.* [2015a] have a similar distribution to that of the entire Hawai‘i data set, and have nearly identical median values ( $43.5 \mu\text{T}$  for our study and *Cromwell et al.* [2015a],  $N=28$ , versus  $44.4 \mu\text{T}$  for all data), but high and low tails in the “All data” CDF curve relative to our results indicate greater variability. The behavior of the Thellier-type and non-Thellier-type CDF curves indicates that the variability in the published data sets manifested in the experimental methodology used to generate the data. The Thellier-type curve is almost entirely shifted to high paleointensity values (median= $54.5 \mu\text{T}$ ,  $N=74$ ) relative to our data, and the non-Thellier-type curve is completely shifted to lower

values (median=38.3  $\mu$ T, N=51) relative to our data. Figure 5b and Figure 5c show CDF curves of non-Thellier-type and Thellier-type data by individual methods. In Figure 5b, the IZZI and Coe-Thellier distributions are very similar to that of our data, although the Coe-Thellier curve is slightly higher. The Thellier-Thellier CDF curve shows the most substantial departure from our dataset, with an exceptional shift toward high values. The pseudo-Thellier, microwave, and MSP-DSC method curves in Figure 5b show some overlap with our data, while the Shaw curve is entirely lower.

One potential cause for differences in the median values between the results in this study and *Cromwell et al.* [2015a], and Thellier-type and non-Thellier-type data is the different site ages investigated with the different techniques. In order to compensate for the differences in age, we plot the median values of all the data for each subset in 500 year bins (Figure 6). In all but one bin (1,500-2,000 yr B.P.), the Thellier-type data have the highest median value while the non-Thellier-type have the lowest. It appears that the differences observed among the various subsets are not due to differences in site ages, but reflect true differences in the data.

Our study and that of *Cromwell et al.* [2015a] used the IZZI experimental method on rapidly cooled, glassy volcanic material, while the Thellier-type and non-Thellier-type experimental techniques are frequently performed on more slowly cooled lava flow interiors. If the difference in observed paleointensity values were based solely on the type of volcanic material, then the Thellier-type and non-Thellier-type data would be expected to have similar paleointensity trends relative to our study and *Cromwell et al.* [2015a], or perhaps have a slightly higher values owing to the slower cooling of the flow interiors relative to the quickly cooled material collected in this study (e.g., *Halgedahl et al.* [1980]), assuming single-domain like behavior: we note that PSD and MD behavior has frequently been shown to not exhibit a cooling rate dependence (e.g., *Yu*

[2011]; *Biggin et al.* [2013]; *Ferk et al.* [2014]). Instead, the Thellier-type data are the highest and the non-Thellier-type data the lowest with our data splitting the difference, indicating that the difference between these two sub-sets must stem from either experimental design or the manner in which the data were selected.

The cause of the discrepancy between our data and the Thellier-type published data (specifically data produced by the Thellier-Thellier method) is difficult to explain. The experimental methodology of the IZZI experiment used in our study and the II and ZI experiments used in the published data are fundamentally similar, yet the II data in particular are consistently higher than ours. Without access to the original measurement level data, it is difficult to assess the role of selection criteria. However, the data set of *Pressling et al.* [2006] (the majority of the II data) used the so-called ‘PICRIT-03’ set of selection criteria of *Kissel and Laj* [2004] which uses a fraction of remanence  $f$  (see *Paterson et al.* [2014] for statistical definition) of 0.35 as a cutoff; this value is substantially smaller than  $FRAC$  in the CCRIT criteria (0.78, see Table 6) used here. The lower fraction of remanence does not exclude samples with Arai plots that are significantly concave-up. If the lower temperature steps of concave-up Arai plots are chosen as the preferred intensity component, then the resulting interpretations could be biased high relative to straight Arai plots.

We examine the specimen results from *Pressling et al.* [2006] to test whether using the PICRIT-03 selection criteria produces substantially higher intensity values for specimens with a low fraction of remanence. In Figure 7a we plot specimen intensity as a function of the fraction of remanence,  $f$ , used in the intensity calculation. “1st class” specimens, defined by *Pressling et al.* [2006] as  $f > 0.5$ , have a median intensity of 60.1  $\mu\text{T}$ , which is  $\sim 4\%$  lower than the median intensity for “2nd class” specimens ( $f < 0.5$ ) of 62.7  $\mu\text{T}$ . Outside of the specimen

class definitions, there is a noticeable trend in the distribution of intensities with regard to  $f$ ; the highest intensity values are only found in specimens with  $f < 0.6$ , and the lowest intensity values are found in specimens with  $f > 0.45$ . Without the original measurement data we cannot verify whether low  $f$  specimens used the first slope of concave-up Arai plots, but the listed temperature ranges in *Pressling et al.* [2006] indicate that this is the likely case.

To test this hypothesis using our own data, we first find all the specimen interpretations from this study and *Cromwell et al.* [2015a] that pass PICRIT-03 but fail CCRIT and show no sign of alteration. We then choose the specimen interpretations with the lowest blocking temperature bounds, under the assumption that they are likely to be biased high, and calculate site mean values. Figure 7b shows the comparison of these PICRIT-03 site mean estimates with those from CCRIT. The plot does not confirm the hypothesis that using PICRIT-03 will result in overall higher estimates, even when choosing only the first slope, although there is a greater amount of variability in the PICRIT-03 estimates compared to the CCRIT estimates. These results indicate that relatively loose selection criteria may not be a contributor to high biases in paleointensity data in all cases, and can not account for the high bias in the II and ZI published results shown in Figure 3. The observations in Figure 7b do support the findings of *Tauxe et al.* [2016], who demonstrated that the CCRIT selection criteria is both more accurate and more precise than other popular selection schemes when comparing paleointensities obtained from samples magnetized in known fields.

Another likely cause of the discrepancy between the II and ZI experimental data and our data is the type of material. The rapidly cooled, glassy volcanic material used in our study and *Cromwell et al.* [2015a] is more likely single-domain and therefore more likely to generate linear Arai diagrams than material sampled from the slowly cooled interiors of lava flows,



which are more likely to be multi-domain. The difficulty here is that, while single domain remanences display a strong dependence on cooling rate (e.g., *Halgedahl et al.* [1980]), our laboratory treatment replicates the original cooling rate for basaltic glasses quite well (e.g., *Bowles et al.* [2005]) and in any case, this phenomenon would overestimate field strength, not underestimate. Moreover, for reasons that are poorly understood, it appears that pseudo-single domain and multi-domain domain states do not have a cooling rate dependence, so the observed overestimates of the  $H_c$  relative to the IZZI experiments would only occur if the lava flow specimens analyzed with the Thellier-Thellier method were in fact single-domain but slowly cooled. Testing this hypothesis requires access to the original measurement data, which are not available in the MagIC database. It is also worth mentioning that *Pressling et al.* [2007] were unable to reproduce the high intensity values published in *Pressling et al.* [2006] when using the microwave method. This observation suggests that perhaps it is the Thellier-Thellier method itself which results in the overestimate by some unknown mechanism, a hypothesis that is beyond the scope of this study.

One reason that published paleointensity data could be biased “low” compared to our data relates to our observation in Figure 4d. The total TRM of this specimen, which has a curved Arai plot but no obvious signs of alteration, gave a much lower field estimate than sister specimens that passed the CCRIT criteria (as in Figure 4c). If this were generally true (as hinted at by *Cromwell et al.* [2013]), then total TRM-based laboratory methods (like the Shaw method) would give site means that are biased low, as these methods do not screen out the failure of reciprocity that results in curved Arai plots. To test this hypothesis, we compare estimates for each site mean based on at least three specimens that passed the CCRIT criteria to total TRM intensities from specimens from the same lava flow that failed CCRIT. We exclude alteration

effects by using a threshold value for  $DRATS < 10$  (see *Paterson et al.* [2014] for definition). Comparing site mean estimates for the same lava flows (Figure 7c) strongly suggests that the total TRMs of specimens that do not pass CCRIT are in fact biased low relative to those that pass CCRIT. These results indicate that the low bias observed in non-Thellier-type data compared to our glassy volcanic data stems from experimental design that does not test for single-domain like behavior, and that total TRM paleointensity methods are likely to underestimate the expected geomagnetic field strength in general.

## 7. Conclusions

- We present high-quality paleointensity results for 22 Holocene lava flows (270 - 6,500 yr B.P.) from the Island of Hawai‘i. We follow the sampling and experimental methodology of *Cromwell et al.* [2015a] by sampling rapidly cooled, glassy material from each lava flow, utilizing the IZZI-Thellier paleointensity experimental method, and implementing strict specimen level selection criteria.
- The new data presented here along with those published by *Cromwell et al.* [2015a] are comparable with published intensity data and for the younger ages are quite consistent with the global paleointensity models CALS10k.2, HFM.OL1.A1 [*Constable et al.*, 2016] and PFM9K [*Nilsson et al.*, 2014]. However, a break-down of the data by technique appears to show that non-Thellier paleointensity methods are significantly lower than our data while those from the Thellier-Thellier technique are significantly higher.
- We have demonstrated here that non single-domain total TRMs are biased low relative to single-domain like remanences from the same lava flows, presenting a likely explanation for the low bias in non-Thellier methods relying on total TRMs for normalization relative to our

IZZI experiments. However, the cause of the high bias observed in the Thellier-Thellier results relative to our IZZI results remains unclear.

- Our results offer no indication of a paleointensity “spike” at  $\sim 3000$  yr B.P., indicating that the exceptionally high field strengths observed in the Levant and elsewhere at this time are not a global phenomenon, at least at the Island of Hawai‘i. There are values very near spike levels at  $\sim 2000$  yr B.P. in our dataset.
- Successful recovery of high-quality paleointensity results from Holocene lava flows on Hawai‘i supports our experimental methodology and is an encouraging beginning for a long-term record intensity record of the Hawaiian islands.

### **Acknowledgments.**

All paleomagnetic data pertaining to this study (including specimen-level intensity estimates, statistics, and experimental measurements) are in the MagIC database at <https://earthref.org/MagIC/DOI/XXXXXX>. L.T. acknowledges support from NSF Grant No. EAR1520674 and EAR1547263. The study was initiated with the help of the US-Israel Binational Science Foundation grant 85739A (H.R. and L.T.) We would also like to thank the insightful and constructive reviews by Ed Mankinen, Huapei Wang, and an anonymous reviewer which substantially improved the manuscript. Any use of trade, firm, or product names is for descriptive purposes only and does not imply endorsement by the U.S. Government.

### **References**

Aitken, M. J., A. L. Allsop, G. D. Bussell, and M. B. Winter (1988), Determination of the intensity of the Earth’s magnetic field during archeological times: reliability of the Thellier technique, *Rev. Geophys.*, 26, 3–12.

- Ben-Yosef, E., L. Tauxe, T. E. Levy, R. Shaar, H. Ron, and M. Najjar (2009), Geomagnetic intensity spike recorded in high resolution slag deposit in Southern Jordan, *Earth and Planetary Science Letters*, 287, 529–539, doi:10.1016/j.epsl.2009.09.001.
- Biggin, A., S. Badejo, E. Hodgson, A. Muxworthy, J. Shaw, and M. Dekkers (2013), The effect of cooling rate on the intensity of thermoremanent magnetization (TRM) acquired by assemblages of pseudo-single domain, multidomain and interacting single-domain grains, *Geophys. J. Int.*, 193, 1239–1249, doi:10.1093/gji/ggt078.
- Bowles, J., J. S. Gee, D. Kent, E. Bergmanis, and J. Sinton (2005), Cooling rate effects on paleointensity estimates in submarine basaltic glass nad implications for dating young flows, *Geochem. Geophys. Geosys.*, 6, Q07,002, doi:10.1029/2004GC000,900.
- Brown, M., F. Donadini, M. Korte, A. Nilsson, K. Korhonen, A. Lodge, S. Lengyel, and C. Constable (2015), GEOMAGIA50.v3 : 1. General structure and modifications to the archeological and volcanic database, *Earth Planets Space*, 67(83), doi:10.1186/s40623-015-0232-0.
- Chauvin, A., P. Roperch, and S. Levi (2005), Reliability of geomagnetic paleointensity data: the effects of the NRM fraction and concave-up behavior on paleointensity determinations by the Thellier method, *Physics of the Earth and Planetary Interiors*, 150, 265–286.
- Coe, R. S. (1967), The determination of paleo-intensities of the Earth's magnetic field with emphasis on mechanisms which could cause non-ideal behavior in Thellier's method, *J. Geomag. Geoelectr.*, 19, 157–178.
- Coe, R. S., S. Grommé, and E. A. Mankinen (1978), Geomagnetic paleointensities from radiocarbon-dated lava flows on Hawaii and the question of the Pacific nondipole low, *J. Geophys. Res.*, 83(B4), 1740–1756, doi:10.1029/JB083iB04p01740.

- Constable, C., M. Korte, and S. Panovska (2016), Persistent high paleosecular variation activity in southern hemisphere for at least 10,000 years, *Earth and Planet. Sci. Lett.*, *453*, 78–86.
- Cottrell, R., and J. Tarduno (1999), Geomagnetic paleointensity derived from single plagioclase crystals, *Earth Planet. Sci. Lett.*, *169*, 1–5.
- Cromwell, G., L. Tauxe, H. Staudigel, C. G. Constable, A. A. P. Koppers, and R. B. Pedersen (2013), In search of long term hemispheric asymmetry in the geomagnetic field: results from high northern latitudes, *Geochemistry Geophysics Geosystems*, *14*(8).
- Cromwell, G., L. Tauxe, H. Staudigel, and H. Ron (2015a), Paleointensity estimates from historic and modern Hawaiian lava flows using glassy basalt as a primary source material, *Physics of the Earth and Planetary Interiors*, *241*, 44–56, doi:10.1016/j.pepi.2014.12.007.
- Cromwell, G., L. Tauxe, and S. Halldorsson (2015b), New paleointensity results from rapidly cooled Icelandic lavas: Implications for Arctic geomagnetic field strength, *Journal of Geophysical Research, Solid Earth*, *120*(5), 2913–2934, doi:10.1002/2014JB011828.
- de Groot, L. V., A. J. Biggin, M. J. Dekkers, C. G. Langereis, and E. Herrero-Bervera (2013), Rapid regional perturbations to the recent global geomagnetic decay revealed by a new Hawaiian record, *Nature Communications*, *4*.
- Dekkers, M., and H. Böhm (2006), Reliable absolute paleointensities independent of magnetic domain state, *Earth Planet. Sci. Lett.*, *248*, 508–517.
- Doell, R., and A. Cox (1972), *The Pacific geomagnetic secular variation anomaly and the question of lateral uniformity in the lower mantle*, pp. 245–284, McGraw-Hill, New York, NY.
- Doell, R., and P. Smith (1969), On the use of magnetic cleaning in paleointensity studies, *Journal of Geomagnetism and Geoelectricity*, *21*(3), doi:10.5636/jgg.21.579.

- Fabian, K., and R. Leonhardt (2010), Multiple-specimen absolute paleointensity determination: An optimal protocol including pTRM normalization, domain-state correction, and alteration test, *Earth and Planetary Science Letters*, 297, 84–94.
- Ferk, A., R. Leonhardt, K. U. Hess, S. Koch, R. Egli, D. Krasa, and D. Dingwell (2014), Influence of cooling rate on the thermoremanence of magnetite grains: Identifying the role of different magnetic domain states, *J. Geophys. Res.*, 119, 1599–1606, doi:10.1002/2013JB010845.
- Gratton, M., J. Shaw, and E. Herrero-Bervera (2005), An absolute palaeointensity record from SOH1 lava core, Hawaii using the microwave technique, *Physics of the Earth and Planetary Interiors*, 148(2-4), 193–214, doi:10.1016/j.pepi.2004.09.009.
- Halgedahl, S., R. Day, and M. Fuller (1980), The effect of cooling rate on the intensity of weak-field TRM in single-domain magnetite, *J. Geophys. Res.*, 85, 3690–3698.
- Herrero-Bervera, E., and J. P. Valet (2009), Testing determinations of absolute paleointensity from the 1955 and 1960 Hawaiian flows, *Earth and Planetary Science Letters*, 287, 420–433, doi:10.1016/j.epsl.2009.08.035.
- Hill, M. J., and J. Shaw (2000), Magnetic field intensity study of the 1960 Kilauea lava flow, Hawaii, using the microwave palaeointensity technique, *Geophys. J. Int.*, 142, 487–504.
- Kirschvink, J. L. (1980), The least-squares line and plane and the analysis of paleomagnetic data, *Geophys. Jour. Roy. Astron. Soc.*, 62(3), 699–718, doi:10.1111/j.1365-246X.1980.tb02601.x.
- Kissel, C., and C. Laj (2004), Improvements in procedure and paleointensity selection criteria (PICRIT-03) for Thellier and Thellier determinations: application to Hawaiian basaltic long cores, *Physics of the Earth and Planetary Interiors*, 147, 155–169, doi:

10.1016/j.pepi.2004.06.010.

Laj, C., and C. Kissel (1999), Geomagnetic field intensity at Hawaii for the last 420 kyr from the Hawaii Scientific Drilling Project core, Big Island, Hawaii, *Jour. Geophys. Res.*, *104*(B7), 15,317–15,338.

Laj, C., C. Kissel, V. Scao, J. Beer, D. Thomas, H. Guillou, R. Muscheler, and W. G. (2002), Geomagnetic intensity and inclination variations at Hawaii for the past 98 kyr from core SOH-4 (Big Island): a new study and a comparison with? existing contemporary data., *Physics of the Earth and Planetary Interiors*, *129*(3-4), 205–243, doi:10.1016/S0031-9201(01)00291-6.

Lockwood, J. (1995), *Mauna Loa Eruptive History?The Preliminary Radiocarbon Record*, vol. Geophysical Monograph 92, pp. 81–94, American Geophysical Union, Washington D.C., doi:10.1029/GM092p0081.

Lockwood, J., and P. Lipman (1980), *Bulletin Volcanologique*, *43*, 609–615, doi:10.1007/BF02597697.

Love, J. J., and C. G. Constable (2003), Gaussian statistics for palaeomagnetic vectors, *Geophys. J. Int.*, *152*, 515–565, doi:10.1046/j.1365-246X.2003.01858.x.

Mankinen, E., and D. Champion (1993), Broad trends in geomagnetic paleointensity on Hawaii during Holocene time, *Journal of Geophysical Research*, *98*(B5), 7959–7976, doi:10.1029/93JB00024.

Nagata, T., Y. Arai, and K. Momose (1963), Secular variation of the geomagnetic total force during the last 5000 years, *J. Geophys. Res.*, *68*, 5277–5282.

Nilsson, A., R. Holme, M. Korte, N. Suttie, and M. Hill (2014), Reconstructing Holocene geomagnetic field variation: new methods, models and implications, *Geophys. J. Int.*, *207*(3), doi:10.1093/gji/ggu120.

- Oishi, Y., H. Tsunakawa, N. Mochizuki, Y. Yamamoto, K. Wakabayashi, and H. Shibuya (2005), Validity of the LTD-DHT Shaw and Thellier palaeointensity methods: a case study of the Kilauea 1970 lava, *Physics of the Earth and Planetary Interiors*, *149*(3), 243–257, doi:10.1016/j.pepi.2004.10.009.
- Paterson, G. A. (2011), A simple test for the presence of multidomain behavior during paleointensity experiments, *J. Geophys. Res.*, *116*(B10104), doi:10.1029/2011JB008369.
- Paterson, G. A., L. Tauxe, A. J. Biggin, R. Shaar, and L. C. Jonestrask (2014), On improving the selection of Thellier-type paleointensity data, *Geochemistry Geophysics Geosystems*, *15*(4), 1180–1192, doi:10.1002/2013GC005135.
- Pavón-Carrasco, F., M. L. Osete, J. Torta, and A. De Santis (2014), A geomagnetic field model for the Holocene based on archaeomagnetic and lava flow data, *Earth and Planet. Sci. Lett.*, *388*, 98–109, doi:10.1016/j.epsl.2013.11.046.
- Pressling, N., C. Laj, C. Kissel, D. Champion, and D. Gubbins (2006), Palaeomagnetic intensities from  $^{14}\text{C}$ -dated lava flows on the Big Island, Hawaii: 0–21 kyr, *Earth and Planetary Science Letters*, *247*, 26–40.
- Pressling, N., M. C. Brown, M. N. Gratton, J. Shaw, and D. Gubbins (2007), Microwave palaeointensities from Holocene age Hawaiian lavas: Investigation of magnetic properties and comparison with thermal palaeointensities, *Physics of the Earth and Planetary Interiors*, *162*, 99–118.
- Reimer, P. J., M. G. L. Baillie, E. Bard, A. Bayliss, J. W. Beck, and C. E. Weyhenmeyer (2004), *Radiocarbon*, *46*(3), 1029–1058, doi:10.1017/S0033822200032999.
- Shaar, R., and L. Tauxe (2013), Thellier Gui: An integrated tool for analyzing data from Thellier-type experiments, *Geochemistry Geophysics Geosystems*, *14*(3), doi:



10.1002/ggge.20062.

- Shaar, R., and L. Tauxe (2015), Instability of thermoremanence and the problem of estimating the ancient geomagnetic field strength from non-single-domain recorders, *Proceedings of the National Academy of Science*, *112*, 11,187–11,192, doi:10.1073/pnas.1507986112.
- Shaar, R., H. Ron, L. Tauxe, R. Kessel, and A. Agnon (2011), Paleomagnetic field intensity derived from non-SD: Testing the Thellier IZZI technique on MD slag and a new bootstrap procedure, *Earth and Planetary Science Letters*, *310*, 213–224, doi:10.1016/j.epsl.2011.08.024.
- Shaar, R., L. Tauxe, H. Ron, Y. Ebert, S. Zuckerman, I. Finkelstein, and A. Agnon (2016), Large geomagnetic field anomalies revealed in Bronze to Iron Age archeomagnetic data from Tel Megiddo and Tel Hazor, Israel, *Earth and Planet. Sci. Lett.*, *442*, 173–185, doi:10.1016/j.epsl.2016.02.038.
- Shaw, J. (1974), A new method of determining the magnitude of the paleomagnetic field application to 5 historic lavas and five archeological samples, *Geophys. J. R. Astron. Soc.*, *39*, 133–141.
- Stuiver, M., et al. (1998a), IntCal98 radiocarbon age calibration, 24,000-0 cal BP, *Radiocarbon*, *40*(3), 1041–1083.
- Stuiver, M., P. Reimer, and T. Braziunas (1998b), High-precision radiocarbon age calibration for terrestrial and marine samples, *Radiocarbon*, *40*(3), 1127–1151.
- Stuiver, M., P. Reimer, and R. Reimer (2005), CALIB 5.0. WWW program and documentation.
- Tanaka, H., and M. Kono (1991), Preliminary Results and Reliability of Palaeointensity Studies on Historical and  $C^{14}$  Dated Hawaiian Lavas, *J. Geomag. Geoelect.*, *43*, 375–388.
- Tanaka, H., J. D. E. Athanassopoulos, J. R. Dunn, and M. Fuller (1995), Paleointensity determinations with measurements at high temperature, *J. Geomag. Geoelectr.*, *47*, 103–113.

- Tauxe, L., and H. Staudigel (2004), Strength of the geomagnetic field in the Cretaceous Normal Superchron: New data from submarine basaltic glass of the Troodos Ophiolite, *Geochem. Geophys. Geosyst.*, 5(2), doi:10.1029/2003GC000635.
- Tauxe, L., and T. Yamazaki (2015), *Paleointensities*, vol. 5, pp. 461–509, 2nd edition ed., Elsevier.
- Tauxe, L., T. Pick, and Y. S. Kok (1995), Relative paleointensity in sediments; a pseudo-Thellier approach, *Geophys. Res. Lett.*, 22, 2885–2888.
- Tauxe, L., J. S. Gee, M. B. Steiner, and H. Staudigel (2013), Paleointensity results from the Jurassic: New constraints from submarine basaltic glasses of ODP Site 801C, *Geochemistry Geophysics Geosystems*, 14(10), doi:10.1002/ggge.20282.
- Tauxe, L., et al. (2016), PmagPy: Software package for paleomagnetic data analysis and a bridge to the Magnetics Information Consortium (MagIC) database, *Geochem. Geophys. Geosyst.*, 17, doi:10.1002/2016GC006307.
- Taylor, J. R. (1997), An Introduction to Error Analysis, *Univ. Sci. Books, Mill Valley, Calif.*, p. 327.
- Teanby, N., C. Laj, D. Gubbins, and M. Pringle (2002), A detailed palaeointensity and inclination record from drill core SOH1 on Hawaii, *Physics of the Earth and Planetary Interiors*, 131(2), 101–140, doi:10.1016/S0031-9201(02)00032-8.
- Thellier, E., and O. Thellier (1959), Sur l'intensité du champ magnétique terrestre dans le passé historique et géologique, *Ann. Geophys.*, 15, 285–378.
- Trusdell, F., and J. Lockwood (2017), Geologic map of the northeast flank of Mauna Loa Volcano, Island of Hawai'i, Hawaii, *U.S. Geological Survey, Scientific Investigations Map 2932-A*, scale 1:50,000, doi:10.3133/sim2932A.

- Trusdell, F., and J. Lockwood (in press), Geologic map of the central-southeast flank of Mauna Loa Volcano, Island of Hawai'i, Hawaii, *U.S. Geological Survey, Scientific Investigations Map 2932-B*, scale 1:50,000.
- Trusdell, F., E. Wolfe, and J. Morris (2006), Digital database of the geologic map of the island of Hawai'i, *U.S. Geological Survey, DS-144*.
- Valet, J. P., E. Tric, E. Herrero-Bervera, L. Meynadier, and J. P. Lockwood (1998), Absolute paleointensity from Hawaiian lavas younger than 35 ka, *Earth and Planetary Science Letters*, *161*, 19–32.
- Vogel, J., J. Southon, D. Nelson, and T. Brown (1984), Performance of catalytically condensed carbon for use in accelerator mass spectrometry, *Nuclear Instruments and Methods in Physics Research Section B: Beam Interactions with Materials and Atoms*, *5*(2), 289–293, doi:10.1016/0168-583X(84)90529-9.
- Walton, D., J. Shaw, J. Share, and J. Hakes (1992), Microwave demagnetization, *J. Appl. Phys.*, *71*, 1549–1551.
- Wang, H., and D. V. Kent (2013), A paleointensity technique for multidomain igneous rocks, *Geochemistry Geophysics Geosystems*, *14*, 4195–4213, doi:doi:10.1002/ggge.20248.
- Wright, T., J. Chun, J. Esposito, C. Heliker, J. Hodge, J. Lockwood, and S. Vogt (1992), Map showing lava-flow hazard zones, Island of Hawaii, *U.S. Geological Survey, Map MF-2193*.
- Yu, Y. (2011), Importance of cooling rate dependence of thermoremanence in paleointensity determination, *J. Geophys. Res.*, *116*, doi:10.1029/2011JB008388.
- Yu, Y., L. Tauxe, and A. Genevey (2004), Toward an optimal geomagnetic field intensity determination technique, *Geochemistry, Geophysics, Geosystems*, *5*(2), Q02H07, doi:10.1029/2003GC000630.

Accepted Article

Zhao, X., Q. Liu, G. Paterson, H. Qin, S. Cai, Y. Yu, and R. Zhu (2014), The effects of secondary mineral formation on Coe-type paleointensity determinations: Theory and simulation, *Geochemistry Geophysics Geosystems*, 15(4), 1215–1234, doi:10.1002/2013gc005165.

Table 1: Locations and ages for all sites sampled as part of this study. Latitude and longitude are in degrees north and east, respectively. Unit is the lava flow unit for each sites as mapped in *Trusdell et al.* [2006], and FID is the flow identifier number from that same study. Site ages are reported in radiocarbon years before present (yr B.P., before the calendar year datum of C.E. 1950). Age uncertainties are in years. Ref is the reference code for radiocarbon dates: (1) *Lockwood* [1995], (2) *Trusdell et al.* [2006], (3) *Trusdell and Lockwood* [2017], (4) *Trusdell and Lockwood* [in press]. Ages for sites marked with an asterisk were estimated from their mapped locations in *Trusdell et al.* [2006] (see text).

Site Name	Latitude (N)	Longitude (E)	Unit	FID	Age (yr B.P.)	Age $\pm$ (yr)	Ref
hw100	19.130795	-155.509045	k1y	5971	3,850	38	1
hw101	19.130903	-155.509505	k1y	5971	3,850	38	1
hw102	19.131035	-155.509676	k1y	5971	3,850	38	1
hw103	19.709897	-155.1339467	k1y	1846	3,404	25	3
hw104	19.766319	-155.940188	h2	1012	2,700		2
hw105	19.784449	-155.90021	h2	1012	2,798	89.4	2
hw106	19.802943	-155.847055	h2	983	2,030		2
hw107	19.903266	-155.889173	h2	870	2,250	750	2*
hw109	19.739374	-156.029435	k1y	684	2,140		2
hw110	19.713514	-156.033525	h2	1534	3,020		2
hw111	19.684601	-156.0349	h1y	1741	3,020		2
hw112	19.659842	-156.008613	h2	1840	2,250		2
hw113	19.57904	-155.943793	h2	2620	2,290		2
hw114	19.156688	-155.506244	k1y	5716	2,920	60	1
hw115	19.150488	-155.510112	k2	5869	2,365	30	1
hw116	19.14252	-155.515005	k1y	5908	2,312	58	1
hw117	19.133598	-155.52049	k2	5927	2,312	58	1
hw118	19.109703	-155.535251	k1y	5991	4,770	90	1
hw119	19.100662	-155.54116	k2	6024	2,475	38	1
hw120	19.094061	-155.54608	k1y	6039	4,770	90	1
hw121	19.064971	-155.613252	k1y	6694	3,393	57	1
hw122	19.059109	-155.689427	k1	6089	6,500	3500	2*
hw124	19.626308	-155.561962	k4	1105	270	60	This study
hw125	19.627499	-155.555155	k2	2349	2,580	320	This study
hw127	19.685337	-155.464169	k5	2009	1,838	94	3
hw129	19.345961	-155.874805	k2	4641	2,280		This study
hw130	19.370954	-155.877186	k2	4080	2,497	63	1
hw131	19.419052	-155.882461	k1y	3985	4,000	1000	2*
hw132	19.4161	-155.880471	k1y	3983	3,270	180	1
hw133	19.429755	-155.91368	k3	3694	2,885	85	This study
hw134	19.457273	-155.918085	k2	3617	2,940	200	1
hw200	19.37027	-154.9552	p2	4516	2,360		2
hw202	19.45116	-154.94109	p3	3803	900		2
hw203	19.99261	-155.23997	ly	528	5,015.7	81.5	2
hw204	19.70004	-155.09063	k3	1871	1,333	26	3

Continued on next page

**Table 1 – continued from previous page**

Site Name	Latitude (N)	Longitude (E)	Unit	FID	Age (yr B.P.)	Age $\pm$ (yrs)	Ref
hw205	19.7101	-155.11478	k1y	1846	3,404	25	3
hw206	19.68752	-155.12013	k1y	2099	4,173	21	3
hw207	19.67905	-155.14202	pha	2157	4,173	21	3
hw208	19.68128	-155.46512	k2	2092	1,838	94	3
hw209	19.23524	-155.47927	k	5546	2,072	37	4
hw210	19.1864	-155.48033	k	5635	9,121	46	4
hw211	19.13435	-155.50505	k1y	5971	3,850	38	1
hw212	19.47184	-155.88969	k4	3412	1,456	58	1
hw213	19.40635	-155.88135	k2	3917	1,819	43	1
hw214	19.42336	-155.0027	k3	3922	1111	51	This study
hw215	19.49376	-155.9183	k4	3099	521	78	1
hw216	19.5177	-155.92037	k2	2423	1,600	200	This study
hw217	19.68449	-155.97262	h1y	2049	3,600		2
hw218	19.739941	-155.97637	h1y	1509	4,700		2
hw219	19.84247	-155.75511	k3	931	1,125	375	2*
hw220	19.83643	-155.7837	k1y	589	3,360	200	This study
hw221	19.78403	-155.90144	h2	983	2,798	89.4	2
hw222	19.72695	-155.41616	ly	1600	4,530		2
hw223	19.72013	-155.43877	ly	1558	5,320		2
hw224	19.62804	-155.5483	k3	2366	1,500	100	3
hw225	19.63142	-155.52462	k3	2074	1,548	83	This study
hw227	19.62987	-155.47922	k4	2137	410	60	3
hw228	19.67202	-155.385	k4	2137	3,433	44	3
hw229	19.89764	-155.88864	k2	6621	1,647	72	This study
hw230	19.79963	-155.9997	h1y	1136	4000	1,000	2*
hw231	19.07474	-155.74713	k3	5999	942	59	1
hw232	19.0607	-155.70472	k2	5839	1,730	60	1
hw233	19.03787	-155.65014	k1y	6694	3,393	57	1
hw234	19.06199	-155.6462	k1y	6694	3,393	57	1
hw235	19.07504	-155.55842	k	6608	<10,000		2*
hw236	19.11537	-155.53176	k3	5978	799	34	1
hw237	19.17623	-155.49034	k1o	5604	9,218	79	4
hw238	19.22239	-155.46153	k3	5593	1,382	35	4
hw239	19.61994	-155.10703	k3	1828	1,470	50	3
hw240	19.61138	-155.03302	k1o	2368	5,455	25	3

Site Name	FID-M/L	Unit Name	Field No.	Lab No.	Quadrant (N/S/E/W)	Latitude (N)	Longitude (E)	Elev. (m)	Age (yr B.P.)	Age C.E. (± 1σ B.P.)	Weighted Avg. (± 1σ B.P.)
hwi/24	413	Kemansu	W86045.61C	W5737	Alomoso	19°51.31'	-155°64.00'	198.2	300 ± 100	1450 to 1952	278 ± 51
hwi/24	413	Kemansu	L79-66	Pu'u Kōhi	19°53.01'	-155°56.20'	224.3	270 ± 60	1458 to 1951	270 ± 60	270 ± 60
hwi/25	61	Kelahi	L-88-66	Pu'u Kōhi	19°53.40'	-155°56.10'	226.8	250 ± 20	1490 to 155	2580 ± 30	2580 ± 30
hwi/29	579	Kelahi	AA10729	Hoponani	19°57.5'	-155°83.88'	245.4	2595 ± 70	170 to 378	2364 ± 59	2364 ± 59

Site Name	FID-ML	Unit Name	Field No.	Lab No.	Quadrangle Name (1:250,000)	Latitude (N)	Longitude (E)	Elev. (m)	Age (yr B.P.)	Age Range (yr C.E.)	Weighted Avg. (yr B.P.)
hw124	413	Kemomku	W6815-61C	W5772	Alumina	19.75131	-155.64400	1728.2	300 ± 100	1429 to 1952	278 ± 51
hw134	413	Kemomku	L-79-66	W4537	Pu'u Koli	19.63017	-155.62301	2243.3	270 ± 60	1458 to 1951	270 ± 60
hw125	61	Piwi 61	L-88-66	W0139	Pu'u Koli	19.63017	-155.62301	2266.8	230 ± 320	1492 to 1951	230 ± 320
hw129	579	Kalahiki	L-91-1105	AA10229	Honouliuli	19.7515	-155.87878	245.5	1530 to 170	1010 to 378	2364 ± 59
hw131	139	Kalahiki	L-91-1105	AA10229	Honouliuli	19.7515	-155.87878	245.5	1530 to 170	1010 to 378	2364 ± 59
hw133	139	Kalahiki	L-97-273	AA4381	Honouliuli	19.45533	-155.91067	71.7	2883 ± 85	1366 to 344	2885 ± 85
hw135	139	Kalahiki	L-97-273	AA4381	Honouliuli	19.45533	-155.91067	71.7	2883 ± 85	1366 to 344	2885 ± 85
hw214	144C	Poumaliu Pigeite	L-89-21	AA5570	Honouliuli	19.42130	-155.90000	85.3	1090 ± 60	778 to 1032	1111 ± 51
hw215	144C	Poumaliu O Honouliuli	L-84-102	W5633	Pu'u Lehua	19.54230	-155.80970	1449.3	1600 ± 200	1710 to 867	1600 ± 200
hw216	144C	Poumaliu	L-84-102	W5633	Pu'u Lehua	19.54230	-155.80970	1449.3	1600 ± 200	1710 to 867	1600 ± 200
hw220	153	Kanirope	L-86-37	W5536	Pu'u Lehua	19.69850	-155.78697	755.9	3300 ± 200	2200 to 1130	3360 ± 200
hw225	63A	Redleg Trail	L-86-37	W5792	Pu'u Lehua	19.69850	-155.54717	1940.1	1500 ± 150	256 to 875	1548 ± 83
hw226	63B	Redleg Trail	L-86-119	W5797	Pu'u Lehua	19.68667	-155.57012	1984.6	1570 ± 100	256 to 653	1647 ± 72
hw229	152	Kamuku	W8064-1-50	W5809	Nihoaue	19.68525	-155.70822	1585.8	1500 ± 100	264 to 763	1647 ± 72
hw229	152	Kamuku	W8064-1-50	AA5671	Nihoaue	19.68520	-155.69070	1795.3	1810 ± 105	42 to 503	

**Table 3.** Radiocarbon ages from *Lockwood* [1995]. Site Name is the paleomagnetic site associated with each  $^{14}\text{C}$  dated lava flow. FID-ML is a unique, three-digit flow identification number assigned to each Mauna Loa mapped surface-flow unit. Age is the resulting age (yr B.P., before the calendar year datum of C.E. 1950) and standard error uncertainty estimates (years) for each lava flow.

Site Name	FID-ML	Unit Name	Age (yr B.P.)
hw100, hw101, hw102, hw211	641	Wailau	$3850 \pm 38$
hw114	634		$2920 \pm 60$
hw115	637	Nīnole A'A	$2365 \pm 30$
hw116, hw117	638	Nīnole Gulch	$2312 \pm 58$
hw118, hw120	751		$4770 \pm 90$
hw119	644	Hōkūkano	$2475 \pm 38$
hw121, hw233, hw234	624	Kauahā'ao Church	$3393 \pm 57$
hw130	680	Kalahiki	$2497 \pm 63$
hw132	686	Kaunene	$3270 \pm 180$
hw134	138	Palemano Point	$2940 \pm 200$
hw212	439	Puu Kinikini	$1456 \pm 58$
hw213	679	Hookena	$1819 \pm 43$
hw215	412	Puu o Uo	$521 \pm 78$
hw224	147	Panaewa Picrite	$1500 \pm 100$
hw231	551	Halepōhāhā	$942 \pm 59$
hw232	545	Pu'u'oke'oke'o	$1730 \pm 60$
hw236	547	Kāwā	$799 \pm 34$



**Table 4.** Radiocarbon ages from *Trusdell et al.* [2006]. Site Name is the paleomagnetic site associated with each  $^{14}\text{C}$  dated lava flow. FID is the lava flow identifier used by *Trusdell et al.* [2006]. C14-N and C14-ID are isotopic sample and age identifiers unique to *Trusdell et al.* [2006]. Age is the resulting age (yr B.P., before the calendar year datum of C.E. 1950) and  $1\sigma$  uncertainty (years). Weighted Avg. ages are weighted by the inverse of their variance before averaging (e.g., *Taylor* [1997]); variance is reported as standard error.

Site Name	FID	C14-N	C14-ID	Age (yr B.P.)	Weighted Avg. (yr B.P.)
hw104	1012	41	41	2700	2700
hw105, 221	983	32	32	$2740 \pm 100$	$2798 \pm 89.4$
hw105, 221	983	33	33	$3030 \pm 200$	
hw106	870	35	35	2030	2030
hw109	1534	40	40	2140	2140
hw110	1741	39	39	3020	3020
hw111	1741	39	39	3020	3020
hw112	1840	29	29	2250	2250
hw113	2620	50	106	2290	2290
hw200	4516	94	157	2360	2360
hw202	3803	95	158	900	900
hw203	528	148	211	$4850 \pm 150$	$5015.7 \pm 81.5$
hw203	528	149	212	$5085 \pm 97$	
hw217	2049	38	38	3600	3600
hw218	1509	43	43	4700	4700
hw222	1600	15	15	4550	4530
hw222	1600			4510	
hw223	1558	60	116	5320	5320

Table 5: Radiocarbon ages from *Trusdell and Lockwood* (2017) and *Trusdell and Lockwood* (in press). All ages are reported in radiocarbon years before present (yr B.P.), before the calendar year datum of C.E. 1950. Materials dated include charcoal, roots, twigs, vegetative litter, or unaltered wood (rarely). Site Name is the paleomagnetic site associated with each  $^{14}\text{C}$  dated lava flow. FID ML is a unique, three-digit flow identification number assigned to each Mauna Loa mapped surface-flow unit. Field No. is the radiocarbon sample ID. Lab No. is the laboratory sample name, where initial letter(s) identify the analytical laboratory: "W" and "TO" is U.S. Geological Survey, IAC Laboratory, Reston, Virginia; "USGS" is U.S. Geological Survey, IAC Laboratory, Menlo Park, California; "A" is University of Arizona, Tucson, Arizona; "SUERC" is Scottish Universities Environmental Research Centre, East Kilbride; AMS ages have the call letters: "A", "WW", "TO", and "SUERC". Latitude and Longitude are sample locations in Universal Transverse Mercator projection; Old Hawaiian Datum. Elev. is the sample elevation in meters. Age is the calibrated sample age with  $2\sigma$  uncertainty. Weighted Avg. ages are weighted by the inverse of their variance before averaging (e.g., *Tinlor* [1997]); variance is reported as standard error. Age Range: each age was calibrated to calendar years using CALIB 6.0 Radiocarbon Calibration Program [Stuiver et al., 2005]; calibrated ages are for 2 $\sigma$ ; entire age range of calendar ages is possible for a given sample; unspecified ages are common em (C.E.), negative (+) ages are before common em (B.C.E.). Ref is the reference code in Table 1; <sup>3</sup> *Trusdell and Lockwood* (2017), <sup>4</sup> *Trusdell and Lockwood* (in press).

Site Name	FID ML	Unit Name	Field No.	Lab No.	Quadrangle Name (1:24,000)	Latitude (N)	Longitude (E)	Elev. (m)	Age (yr B.P.)	Age Range (yr C.E.)	Weighted Avg. (yr B.P.)	Ref
hw103.205	863	Punahoa flow	L-82-33	W5112	Upper P <sup>h</sup> thoma	19.70961	-155.27281	1104.9	3110 ± 60	-1505 to -1213	3404 ± 25	3
hw103.205	863	Punahoa flow	HCB-79-19	W4621	Hilo	19.70522	-155.11671	169.2	3140 ± 70	-1606 to -1215		3
hw103.205	863	Punahoa flow	HCB-79-55	W4629	Hilo	19.69773	-155.12492	216.4	3360 ± 80	-1879 to -1462		3
hw103.205	863	Punahoa flow	PCB-49-78	W4624	P <sup>h</sup> thoma	19.71529	-155.13588	256.0	3380 ± 80	-1885 to -1499		3
hw103.205	863	Punahoa flow	PCB-49-107	W4630	Hilo	19.71338	-155.13513	298.7	3420 ± 60	-1920 to -1618		3
hw103.205	863	Punahoa flow	HCB-79-33R	W4631	Hilo	19.71507	-155.13513	340.0	3450 ± 60	-1920 to -1618		3
hw103.205	863	Punahoa flow	L-92-20E	WW849	P <sup>h</sup> thoma	19.71610	-155.15150	329.2	3660 ± 60	-2201 to -1889		3
hw103.205	863	Punahoa flow	L-79-67	W4574	P <sup>h</sup> thoma	19.71801	-155.13851	263.0	3700 ± 70	-2290 to -1899		3
hw127.208	866	Po'u Kāhikihi flow	L-86-156	W5985	Po'u O'o	19.69001	-155.46750	2011.7	1580 ± 120	173 to 668	1838 ± 94	3
hw127.208	866	Po'u Kāhikihi flow	L-84-32	W5566	Po'u O'o	19.70170	-155.39007	1741.9	2240 ± 150	-758 to 49		3
hw204	829	Kikinau flow	HCB-79-39	W4631	Hilo	19.70639	-155.08611	41.1	1110 ± 60	778 to 1022	1333 ± 26	3
hw204	829	Kikinau flow	HB-79-53A	W5597	Hilo	19.71575	-155.09520	45.7	1140 ± 300	260 to 1409		3
hw204	829	Kikinau flow	L-78-34	W4343	Hilo	19.69669	-155.12245	231.6	1280 ± 70	639 to 936		3
hw204	829	Kikinau flow	L-78-113	W4237	Kūlanī	19.56323	-155.34484	1883.7	1320 ± 50	618 to 856		3
hw204	829	Kikinau flow	Kūa-116	W4340	Kūlanī	19.59510	-155.34744	1778.5	1400 ± 70	442 to 776		3
hw204	829	Kikinau flow	Kūa-116	W4357	Kūlanī	19.58410	-155.34855	1812.0	1490 ± 50	433 to 650		3
hw206.207	854	Wilder Road flow	HCB-85-06	W5870	Hilo	19.66473	-155.12256	237.7	1500 ± 200	88 to 968		3
hw206.207	854	Wilder Road flow	Kūa-117	W5870	Kūlanī	19.58460	-155.34485	1816.7	4070 ± 70	-2872 to -2511	4173 ± 21	3
hw206.207	854	Wilder Road flow	W5870	W5870	P <sup>h</sup> thoma	19.58460	-155.34485	1816.7	4070 ± 70	-2872 to -2511		3
hw206.207	854	Wilder Road flow	L-81-22	W4693	P <sup>h</sup> thoma	19.69175	-155.15303	371.9	4210 ± 80	-3011 to -2495		3
hw206.207	854	Wilder Road flow	L-81-22R	SUERC-5410	P <sup>h</sup> thoma	19.69175	-155.15303	371.9	4210 ± 80	-2869 to -2582		3
hw206.207	854	Wilder Road flow	L-96-01	WW880	Hilo	19.72380	-155.08780	21.3	4410 ± 60	-3334 to -2906		3
hw209	295	Red Cone flow	HCB-81-45	W5077	Hilo	19.69048	-155.12012	182.9	4410 ± 120	-3497 to -2701		3
hw209	295	Red Cone flow	77L-56*	W4161	Keaiawa Reservoir	19.29650	-155.57000	2060.4	2000 ± 70	-195 to 131	2072 ± 37	4
hw209	295	Red Cone flow	77L-57*	W4163	Keaiawa Reservoir	19.31000	-155.56200	2036.1	1980 ± 80	-195 to 227		4
hw209	295	Red Cone flow	L-91-186*	W6349	Keaiawa Reservoir	19.31070	-155.58880	2292.1	2150 ± 50	-364 to -45		4
hw210	383	Ke'u High flow	L-93-101	WW339	Pihala	19.20270	-155.47933	298.7	8720 ± 70	-8166 to -7589	9121 ± 46	4
hw210	383	Ke'u High flow	L-91-50	AA7656	Pihala	19.21100	-155.47970	297.2	8955 ± 115	-8425 to -7715		4
hw210	383	Ke'u High flow	L-91-680	W4882	Pihala	19.20817	-155.49070	353.6	9960 ± 170	-10771 to -8878		4
hw210	383	Ke'u High flow	L-93-533*	W3343	Pihala	19.21967	-155.50750	644.7	9540 ± 80	-9213 to -8653		4
hw227	862	Punahoa flow	L-81-58	W5879	Po'u O'o	19.66473	-155.46599	2038.9	1010 ± 60	1419 to 1653		3
hw228	868	Kikinau flow	L-84-79R	W5666	Upper P <sup>h</sup> thoma	19.69175	-155.15303	371.9	4210 ± 80	-3011 to -2495		3
hw228	868	Kikinau flow	L-84-79R	W5666	Upper P <sup>h</sup> thoma	19.69175	-155.15303	371.9	4210 ± 80	-3011 to -2495		3
hw237	742	Lae O Pihali flow	9PT0C1	W3715	Upper P <sup>h</sup> thoma	19.71550	-155.31770	1313.7	3415 ± 45	-1879 to -1615	3433 ± 44	3
hw237	742	Lae O Pihali flow	78L-18*	W4419	Pihala	19.16267	-155.40750	64.0	9300 ± 130	-9118 to -8261	9218 ± 79	4
hw238	288	Ka'ala'ala Gulch flow	77L-17A	W4201	Punahoa	19.20733	-155.53800	652.3	1970 ± 100	-8694 to -8227	1382 ± 35	4
hw238	288	Ka'ala'ala Gulch flow	77L-17B	W3857	Pihala	19.22383	-155.46570	362.7	1470 ± 60	433 to 661		4
hw238	288	Ka'ala'ala Gulch flow	9WV2C	W3858	Pihala	19.22383	-155.46570	362.7	1400 ± 60	541 to 770		4
hw238	288	Ka'ala'ala Gulch flow	MI-87-C5	W4430	Wood Valley	19.26750	-155.48530	688.8	1270 ± 70	645 to 940		4
hw239	828	Puna'ewa pterite flow	L-81-54	W6037	Pihala	19.22850	-155.46630	359.7	1290 ± 120	543 to 994		4
hw240	947	Po'u Maka'ala pterite flow	L-79-37	W4981	Hilo	19.64286	-155.05660	109.7	1470 ± 50	436 to 659	1470 ± 50	3
hw240	947	Po'u Maka'ala pterite flow	L-79-37	W4536	Mountain View	19.61100	-155.03200	97.5	5250 ± 100	-4330 to -3806	5455 ± 25	3
hw240	947	Po'u Maka'ala pterite flow	L-79-37R	WW3712	Mountain View	19.61100	-155.03200	97.5	5480 ± 30	-4435 to -4260		3

**Table 6.** Specimen and site level selection criteria for CCRIT [Cromwell *et al.*, 2015a] and PICRIT-03 Kissel and Laj [2004] selection methods. For the SCAT criterion in CCRIT, the  $\beta_{threshold}$  value is 0.1. See Paterson *et al.* [2014] for detailed descriptions of each statistic.

CCRIT									
<i>Specimen</i>							<i>Site</i>		
SCAT	FRAC	Gap Max	$\beta$	$MAD_{free}$	DANG	$ \vec{k}' $	$nn$	$B_\sigma$	$B_\sigma$ %
TRUE	$\geq 0.78$	$\leq 0.60$	$\leq 0.10$	$\leq 5.0^\circ$	$\leq 10.0^\circ$	$\leq 0.164$	$\geq 3$	$\leq 4 \mu T$	$\leq 10$ %

PICRIT-03									
<i>Specimen</i>						<i>Site</i>			
$f$	$\beta$	$q$	DRAT	CDRAT	MAD	$nn$	$B_\sigma$	%	
$\geq 0.35$	$\leq 0.1$	$\geq 0.20$	$\leq 7$ %	$\leq 10$ %	$\leq 7.0^\circ$	$\geq 3$	25	%	

**Table 7.** Paleointensity results for all sites meeting selection requirements. All ages are reported in radiocarbon years before present (yr B.P., before the calendar year datum of C.E. 1950).  $nn$  is the number of successful specimens per site.  $B_F$  is the estimated ancient field strength in microTesla,  $B_\sigma$  is the standard deviation of  $B_F$ , and  $B_F\%$  is percent error of each estimate. VADM (virtual axial dipole moment) and VADM  $\sigma$  values are in ZAm<sup>2</sup>.

Site	Latitude (N)	Longitude (E)	Age (BP)	$nn$	$B_F$	$B_F\sigma$	$B_F\%$	VADM	VADM $\sigma$
hw100	19.1308	-155.5090	3850 $\pm$ 38	11	37.8	3.1	8.06	85.0	7.0
hw103	19.7099	-155.1339	3404 $\pm$ 25	6	58.8	0.7	1.15	131.0	1.5
hw104	19.7663	-155.9402	2700	8	58.9	5.3	8.91	131.0	11.7
hw105	19.7844	-155.9002	2798 $\pm$ 89.4	3	49.2	0.4	0.84	110.0	0.9
hw112	19.6598	-156.0086	2250	5	55.8	3.6	6.43	125.0	8.0
hw118	19.1097	-155.5353	4770 $\pm$ 90	8	51.3	2.4	4.68	115.0	5.4
hw121	19.0650	-155.6133	3393 $\pm$ 57	8	47.5	4.1	8.58	106.9	9.2
hw122	19.0591	-155.6894	6500 $\pm$ 3500	7	42.3	3.9	9.24	95.2	8.8
hw124	19.6263	-155.5620	270 $\pm$ 60	4	42.0	3.0	7.2	93.9	6.8
hw133	19.4298	-155.9137	2885 $\pm$ 85	4	40.0	0.5	1.21	89.6	1.1
hw134	19.4574	-155.9181	2940 $\pm$ 200	5	41.7	0.6	1.54	93.4	1.4
hw204	19.7000	-155.0906	1333 $\pm$ 26	5	46.8	4.2	8.94	105.0	9.3
hw208	19.6813	-155.4651	1838 $\pm$ 94	4	67.1	1.2	1.81	150.0	2.7
hw209	19.2352	-155.4793	2072 $\pm$ 37	5	35.0	2.4	6.94	78.6	5.5
hw214	19.4234	-155.9003	1111 $\pm$ 51	3	40.0	0.3	0.73	89.6	0.7
hw224	19.6292	-155.5483	1500 $\pm$ 100	3	50.1	3.8	7.56	112.0	8.5
hw225	19.6314	-155.5246	1548 $\pm$ 83	4	38.7	2.4	6.27	86.5	5.4
hw228	19.6724	-155.3853	3433 $\pm$ 44	4	45.1	4.5	9.99	101.0	10.1
hw229	19.8976	-155.8886	1647 $\pm$ 72	4	67.3	6.2	9.2	150.0	13.8
hw230	19.7996	-155.9997	4000 $\pm$ 1000	10	47.4	3.2	6.77	106.0	7.2
hw231	19.0746	-155.7469	942 $\pm$ 59	5	49.9	4.9	9.84	112.0	11.0
hw239	19.6199	-155.1070	1470 $\pm$ 50	3	52.1	3.5	6.74	116.0	7.9

Table 8: Paleointensity results for all specimens meeting selection requirements.  $F$  is the measured intensity in microTesla,  $T_{low}$  and  $T_{high}$  are lower and upper temperature bounds used to calculate intensity, and  $n$  and  $n_{pTRM}$  are the number of temperature steps and pTRM checks used in that same calculation.  $SCAT$ ,  $FRAC$ ,  $GAP$ ,  $Max$ ,  $\beta$ ,  $MAD_{free}$ ,  $DANG$ , and  $|k'|$  are statistics used to determine specimen reliability. See “Selection Criteria” section for a description of all statistics, and Table 6 for selection criteria.

Specimen	Site	$F$	$T_{low}$	$T_{high}$	$n$	$n_{pTRM}$	$SCAT$	$FRAC$	$GAP$	$Max$	$\beta$	$MAD_{free}$	$DANG$	$ k' $
hw100a2	hw100	39.47	0	500	15	6	Pass	0.98	0.45	0.02	0.02	1.19	1.34	0.15
hw100a1	hw100	38.82	0	325	8	3	Pass	0.81	0.47	0.02	0.02	1.98	3.15	0.07
hw100a5	hw100	34.93	0	325	8	3	Pass	0.8	0.52	0.01	0.01	1.76	3.6	0.06
hw100b2	hw100	46.04	0	300	7	2	Pass	0.87	0.57	0.04	0.04	0.84	3.95	0.06
hw100a4	hw100	35.79	0	275	6	2	Pass	0.82	0.58	0.01	0.01	1.21	3.19	0.05
hw100a3	hw100	37.26	0	325	8	3	Pass	0.81	0.54	0.01	0.01	1.25	2.21	0
hw211a5	hw100	37.85	0	350	7	2	Pass	0.8	0.44	0.02	0.02	3.09	9.99	0
hw211b2	hw100	35.61	100	540	15	7	Pass	0.89	0.28	0.03	0.03	2.46	2.53	0
hw211b5	hw100	35.32	100	550	16	7	Pass	0.9	0.21	0.02	0.02	4.93	2.81	0
hw211a3	hw100	37.34	0	350	7	2	Pass	0.79	0.46	0.04	0.04	2.43	7.99	0
hw211a2	hw100	38.35	0	375	8	3	Pass	0.79	0.31	0.03	0.03	4.19	7.25	0
hw103c2	hw103	57.78	100	350	8	3	Pass	0.79	0.35	0.01	0.01	1.03	0.32	0
hw103b1	hw103	59.71	0	325	8	3	Pass	0.78	0.41	0.07	0.07	1.52	2.55	0.02
hw103c5	hw103	58.69	100	275	5	2	Pass	0.84	0.37	0.02	0.02	1.26	2.36	0.1
hw103c1	hw103	59.25	0	350	9	3	Pass	0.89	0.35	0.02	0.02	1.47	0.39	0.11
hw103c3	hw103	58.35	100	425	11	5	Pass	0.97	0.27	0.02	0.02	0.75	0.25	0.15
hw103c4	hw103	58.86	200	375	8	4	Pass	0.88	0.31	0.02	0.02	0.88	0.35	0.16
hw104c4	hw104	57.65	0	525	16	7	Pass	0.79	0.15	0.03	0.03	3.27	3.65	0.16
hw104a4	hw104	59.12	0	565	18	8	Pass	0.99	0.25	0.03	0.03	1.14	0.77	0.1
hw104a1	hw104	62.38	0	525	16	7	Pass	0.96	0.23	0.04	0.04	1.1	0.96	0.08
hw104a2	hw104	63.23	0	565	18	8	Pass	0.97	0.18	0.02	0.02	2.78	1.44	0.07
hw104c5	hw104	47.27	0	580	19	8	Pass	0.99	0.17	0.03	0.03	2.43	1.15	0.03
hw104a5	hw104	63.89	0	500	15	6	Pass	0.93	0.24	0.05	0.05	1.48	0.74	0.02
hw104b4	hw104	58.66	100	500	14	6	Pass	0.85	0.15	0.02	0.02	3.09	2.34	0
hw104b5	hw104	58.73	100	500	14	6	Pass	0.88	0.13	0.03	0.03	1.69	2.96	0.16
hw105a1	hw105	49.5	0	525	16	7	Pass	0.93	0.19	0.03	0.03	2.91	4.05	0.14

Continued on next page

Table 8 – continued from previous page

Specimen	Site	$F$	$T_{low}$	$T_{high}$	$n$	$n_{pTRM}$	SCAT	FRAC	Gap Max	$\beta$	$MAD_{free}$	DANG	$ k' $
hw105a5	hw105	49.38	0	350	9	3	Pass	0.8	0.21	0.03	0.7	0.22	0.04
hw105a4	hw105	48.73	100	450	12	5	Pass	0.81	0.18	0.03	1.39	1.23	0.1
hw112a3	hw112	61.79	0	350	9	3	Pass	0.79	0.4	0.03	0.95	2.49	0.12
hw112a4	hw112	55.7	0	425	12	5	Pass	0.91	0.41	0.02	3.04	1.61	0.1
hw112a1	hw112	55.15	200	350	7	3	Pass	0.81	0.54	0.05	1.39	2.19	0.05
hw112b1	hw112	52.42	0	400	10	4	Pass	0.8	0.18	0.01	4.37	6.95	0.05
hw112b4	hw112	53.89	0	400	10	4	Pass	0.82	0.24	0.02	4.64	8.12	0.05
hw120a3	hw118	51.46	0	580	19	8	Pass	0.99	0.37	0.02	0.88	1.17	0.15
hw120a1	hw118	48.98	0	425	12	5	Pass	0.82	0.31	0.05	4.68	1.6	0.15
hw120a5	hw118	52.91	0	550	17	7	Pass	0.99	0.33	0.02	1.31	0.78	0.13
hw118a4	hw118	51.21	0	325	8	3	Pass	0.9	0.58	0.04	1.29	1.27	0.12
hw120a2	hw118	51.24	0	450	13	5	Pass	0.85	0.42	0.02	1.81	2.4	0.09
hw118b5	hw118	52.89	0	375	9	3	Pass	0.96	0.42	0.03	3.34	1.85	0.07
hw118a1	hw118	51.72	0	400	11	4	Pass	0.88	0.44	0.03	2.27	8.17	0.07
hw118b4	hw118	51.54	0	375	9	3	Pass	0.95	0.45	0.03	2.97	1.05	0.01
hw118b2	hw118	50.83	0	300	6	2	Pass	0.87	0.51	0.04	2.55	1.02	0
hw118b3	hw118	45.8	0	300	6	2	Pass	0.88	0.55	0.02	1.24	0.9	0
hw118b1	hw118	50.52	0	375	9	3	Pass	0.9	0.46	0.04	2.79	1.42	0
hw118a2	hw118	56.1	0	275	6	2	Pass	0.89	0.53	0.04	1.73	1.4	0.12
hw121a1	hw121	43.62	0	325	8	3	Pass	0.79	0.45	0.02	1.47	4.91	0.08
hw121a5	hw121	43.81	100	400	10	4	Pass	0.8	0.44	0.03	4.76	4.71	0
hw234a4	hw121	51.18	0	325	9	3	Pass	0.91	0.35	0.03	1.57	1.88	0
hw234b3	hw121	47.07	0	300	8	3	Pass	0.8	0.28	0.02	1.96	2.3	0
hw234a3	hw121	46.24	0	300	8	3	Pass	0.8	0.29	0.06	1.96	3.68	0
hw234a1	hw121	55.83	0	325	9	3	Pass	0.84	0.24	0.05	2.67	2.65	0
hw121b4	hw121	46.75	0	350	8	3	Pass	0.89	0.43	0.02	1.82	2.88	0.04
hw121b3	hw121	44.55	0	375	9	3	Pass	0.86	0.42	0.02	1.97	2.78	0.04
hw122b2	hw122	42.91	0	425	11	4	Pass	0.88	0.3	0.03	1.94	6.84	0.14
hw122b5	hw122	46.79	0	425	11	4	Pass	0.85	0.26	0.03	1.85	8.88	0.14
hw122a5	hw122	35.02	100	400	9	4	Pass	0.79	0.36	0.03	2.78	2.27	0
hw122c5	hw122	42.92	100	400	9	4	Pass	0.79	0.17	0.02	2.18	0.69	0
hw122c4	hw122	41.84	100	425	10	4	Pass	0.85	0.15	0.01	1.86	1.38	0.04

Continued on next page

Table 8 – continued from previous page

Specimen	Site	$F$	$T_{low}$	$T_{high}$	$n$	$n_{pTRM}$	SCAT	FRAC	Gap Max	$\beta$	$MAD_{free}$	DANG	$ \vec{k}' $
hw122b1	hw122	46.11	0	325	7	2	Pass	0.85	0.59	0.04	1.43	1.74	0.13
hw122c3	hw122	40.58	100	425	10	4	Pass	0.85	0.15	0.02	1.55	1.59	0.14
hw124b1	hw124	37.6	0	400	11	4	Pass	0.8	0.27	0.02	2.73	5.43	0.15
hw124b4	hw124	43.67	0	375	10	4	Pass	0.79	0.22	0.02	1.58	1.52	0
hw124b5	hw124	44.22	0	350	9	3	Pass	0.79	0.3	0.02	1.83	3.21	0.03
hw124b2	hw124	42.62	0	400	11	4	Pass	0.82	0.27	0.03	3.07	4.41	0.05
hw133a5	hw133	39.84	0	375	10	4	Pass	0.82	0.53	0.03	2.51	6.96	0.11
hw133c4	hw133	40.59	0	425	11	4	Pass	0.91	0.36	0.01	1.16	1.09	0.01
hw133c1	hw133	39.45	0	425	11	4	Pass	0.9	0.39	0.01	1.87	2.66	0.1
hw133c3	hw133	40.12	0	400	10	4	Pass	0.93	0.39	0.03	1.9	2.43	0.16
hw134a1	hw134	41.47	0	375	10	4	Pass	0.82	0.51	0.03	3.08	2.18	0
hw134a3	hw134	42.81	0	500	15	6	Pass	0.93	0.51	0.03	1.94	6.07	0
hw134b1	hw134	41.35	0	325	7	2	Pass	0.88	0.6	0.04	1.48	3.57	0
hw134b2	hw134	41.69	0	300	6	2	Pass	0.89	0.57	0.04	1.62	5.72	0
hw134b3	hw134	41.2	0	300	6	2	Pass	0.84	0.58	0.03	1.71	6.9	0
hw204b1	hw204	48.52	0	275	7	2	Pass	0.89	0.39	0.02	2.15	3.95	0.06
hw204b5	hw204	50.74	0	325	9	3	Pass	0.8	0.28	0.03	2.14	2.54	0
hw204b3	hw204	44.8	100	325	8	3	Pass	0.78	0.37	0.02	1.7	3.98	0.02
hw204b2	hw204	49.53	0	325	9	3	Pass	0.82	0.26	0.02	2.08	0.95	0.07
hw204b4	hw204	40.47	0	275	7	2	Pass	0.85	0.4	0.02	1.36	3.76	0.15
hw208b1	hw208	65.61	250	550	13	8	Pass	0.82	0.13	0.01	1.74	1.44	0.11
hw208b4	hw208	67.09	325	525	9	7	Pass	0.8	0.2	0.02	2.43	1.12	0.13
hw208b3	hw208	67.25	250	525	12	7	Pass	0.83	0.18	0.02	1.74	1.3	0.14
hw208b5	hw208	68.57	225	475	11	6	Pass	0.8	0.25	0.02	2.54	3.83	0.14
hw209b1	hw209	33.92	100	515	13	6	Pass	0.92	0.28	0.02	2.69	0.64	0.06
hw209b5	hw209	33.59	0	400	9	3	Pass	0.78	0.35	0.02	2.19	5.41	0.04
hw209c3	hw209	38.94	0	350	7	2	Pass	0.86	0.59	0.02	3.14	6.45	0.02
hw209a1	hw209	35.83	100	400	11	5	Pass	0.78	0.16	0.02	1.98	1.24	0.12
hw209b3	hw209	32.92	100	550	16	7	Pass	0.92	0.27	0.01	1.58	1.51	0.14
hw214bd	hw214	39.64	100	525	15	7	Pass	0.84	0.23	0.03	1.09	0.69	0.11
hw214b4	hw214	40.21	0	580	20	9	Pass	0.89	0.16	0.02	4.54	0.89	0
hw214b1	hw214	40.04	100	500	12	5	Pass	0.88	0.21	0.04	2.26	2.98	0.04

Continued on next page

Table 8 – continued from previous page

Specimen	Site	$F$	$T_{low}$	$T_{high}$	$n$	$n_{pTRM}$	SCAT	FRAC	Gap Max	$\beta$	$MAD_{free}$	DANG	$ k' $
hw224b3	hw224	52.34	0	350	10	4	Pass	0.82	0.56	0.04	0.79	4.14	0.16
hw224b2	hw224	45.72	0	275	7	2	Pass	0.78	0.5	0.03	1.05	4.93	0.15
hw224b1	hw224	52.22	0	325	9	3	Pass	0.78	0.6	0.03	1.24	1.71	0.14
hw225a4	hw225	39.19	0	475	15	6	Pass	0.93	0.3	0.03	1.85	1.21	0
hw225a5	hw225	39.75	0	425	13	5	Pass	0.87	0.29	0.04	1.58	0.9	0
hw225c1	hw225	40.6	0	475	15	6	Pass	0.89	0.58	0.03	4.32	5.39	0
hw225c2	hw225	35.14	0	325	9	3	Pass	0.85	0.55	0.03	1.1	4.69	0.13
hw228c4	hw228	51.56	0	275	7	2	Pass	0.84	0.33	0.06	2.08	8.82	0.13
hw228ba	hw228	44.65	0	550	17	7	Pass	0.98	0.2	0.03	3.1	0.57	0.03
hw228b3	hw228	41.5	0	325	9	3	Pass	0.81	0.32	0.04	2.11	5.32	0
hw228b4	hw228	42.65	0	425	13	5	Pass	0.8	0.23	0.05	4.36	5.85	0
hw229c3	hw229	63.61	100	500	15	7	Pass	0.95	0.26	0.03	3.27	1.82	0.16
hw229c1	hw229	74.25	350	500	7	6	Pass	0.79	0.28	0.04	2.07	1.03	0.16
hw229a4	hw229	60.78	100	450	13	6	Pass	0.83	0.35	0.04	4.59	7.03	0.14
hw229c4	hw229	70.57	325	525	9	7	Pass	0.78	0.2	0.02	2.06	1.02	0.13
hw230c5	hw230	49.2	200	525	14	7	Pass	0.88	0.18	0.02	3.66	0.82	0.16
hw230a3	hw230	46.86	0	450	14	6	Pass	0.87	0.16	0.03	3.05	1.34	0.16
hw230a1	hw230	42.61	200	475	12	6	Pass	0.81	0.16	0.02	2.67	3.15	0.16
hw230b1	hw230	50.81	100	525	16	7	Pass	0.92	0.18	0.02	1.35	0.89	0.13
hw230a2	hw230	41.15	150	475	13	6	Pass	0.87	0.16	0.03	4.97	1.74	0.12
hw230c1	hw230	49.28	275	525	11	7	Pass	0.8	0.23	0.02	1.87	0.28	0.11
hw230c3	hw230	47.73	150	475	13	6	Pass	0.88	0.18	0.02	1.84	0.87	0.11
hw230b5	hw230	50.8	0	450	14	6	Pass	0.93	0.18	0.02	3.03	1.17	0.1
hw230b3	hw230	47.73	225	525	13	7	Pass	0.79	0.15	0.01	1.74	1.44	0.06
hw230a5	hw230	47.56	150	475	13	6	Pass	0.9	0.19	0.01	3.23	2.28	0.05
hw231ab	hw231	49.95	100	550	16	7	Pass	0.93	0.11	0.03	2.97	0.45	0.13
hw231a6	hw231	51.98	200	500	13	7	Pass	0.81	0.19	0.03	2.25	2.46	0.1
hw231a3	hw231	52.43	150	325	7	3	Pass	0.78	0.25	0.02	1.65	1.58	0.08
hw231a2	hw231	41.41	200	525	14	7	Pass	0.79	0.14	0.04	4.25	4.83	0
hw231a7	hw231	53.58	150	350	8	4	Pass	0.78	0.27	0.03	1.74	1.27	0.04
hw239a5	hw239	55.61	0	550	18	8	Pass	0.96	0.1	0.02	4.76	2.09	0.13
hw239a3	hw239	48.58	100	550	17	8	Pass	0.89	0.12	0.01	4.86	3.25	0.08

Continued on next page



Table 8 – continued from previous page

Specimen	Site	$F$	$T_{low}$	$T_{high}$	$n$	$n_{pTRM}$	SCAT	FRAC	Gap	Max	$\beta$	$MAD_{free}$	DANG	$ \vec{k}' $
hw239a1	hw239	52.12	150	550	16	8	Pass	0.87	0.13		0.03	3.22	2.26	0

**Figure 1.** Locations of Holocene lava flows on the Island of Hawai‘i. Sites are grouped by region; see Table 1 for site specific location and age information. Volcanic centers are plotted as gray triangles.

**Figure 2.** Photos of typical lava flows: a) exposed pahoehoe structure (hw103c); b) aa spires (hw223c); c) broken pahoehoe ropes, inset shows sampled section (hw120a).

**Figure 3.** Paleointensity results for Hawaiian lava flows. Results from this study (red squares) are plotted with  $1\sigma$  error bars, age uncertainties are listed in Table 7. Previously published paleointensity results and age estimates for the last 6,000 years are colored according to experiment type. Global paleointensity model curves CALS10k.2, HFM.OL1.A1 [Constable *et al.*, 2016] and PFM9K [Nilsson *et al.*, 2014], yellow, black, and red lines, respectively.

**Figure 4.** Representative specimen results. Arai plots from IZZI-modified Thellier-Thellier experiments are shown with inset Zijdeveld diagrams and NRM-decay/TRM-growth curves. In the Arai plots: temperature steps are listed in degrees Celsius; pTRM checks are shown as green triangles; in-field/zero-field (IZ) heating steps are shown as blue dots and zero-field/in-field (ZI) are in red; the green lines for a-c are the least-squares component over selected temperature steps for specimens that passed all selection criteria; for d) it is the slope of the total TRM.  $B_F$  values are the estimated ancient field strengths. X-axes in the Zijdeveld diagrams are rotated to the specimen declination. NRM-decay curves are shown in blue, TRM-growth curves are in red.

**Figure 5.** Cumulative distribution function (CDF) curves for different paleointensity experimental methods of Hawaiian intensity data. a) CDFs of IZZI results for glassy basalts from this study and *Cromwell et al.* [2015a] (TS & C15), all Hawai'i data, and published data subsets for Thellier-type and non-Thellier type data (see text for description of methods). b) CDFs of individual Thellier-type experimental methods: Thellier-Thellier (II), Coe-Thellier (ZI), and IZZI. c) CDFs of individual non-Thellier-type experimental methods: pseudo-Thellier (PT), microwave (MW), multispecimen (MSP-DSC), and Shaw (S).

**Figure 6.** Median values of Hawai'i paleointensity data shown in Figure 5, in 500 year bins. Only binned values based on at least three sites are shown. IZZI results for glassy basalts from this study and *Cromwell et al.* [2015a], all Hawai'i data, and published data subsets for Thellier-type and non-Thellier type data (see text for description of methods).

**Figure 7.** Examination of PICRIT-03, CCRIT, and total TRM intensity results. a) Specimen intensities from *Pressling et al.* [2006] plotted as a function of the fraction of remanence,  $f$ , used to calculate intensity. Horizontal black lines represent median intensity values for “1st class” ( $f > 0.5$ , teal symbols) and “2nd class” ( $f < 0.5$ , tan symbols) specimens [*Pressling et al.*, 2006]. c) Site mean paleointensity estimates from this study and *Cromwell et al.* [2015a] that passed CCRIT criteria compared to mean results of specimens from the same sites that failed CCRIT but did not alter during the heating experiment; mean results based on total TRM (b) and the first slope that passes the PICRIT-03 criteria (c). Black line in b) and c) is 1:1 ratio.

Figure 1.

Accepted Article

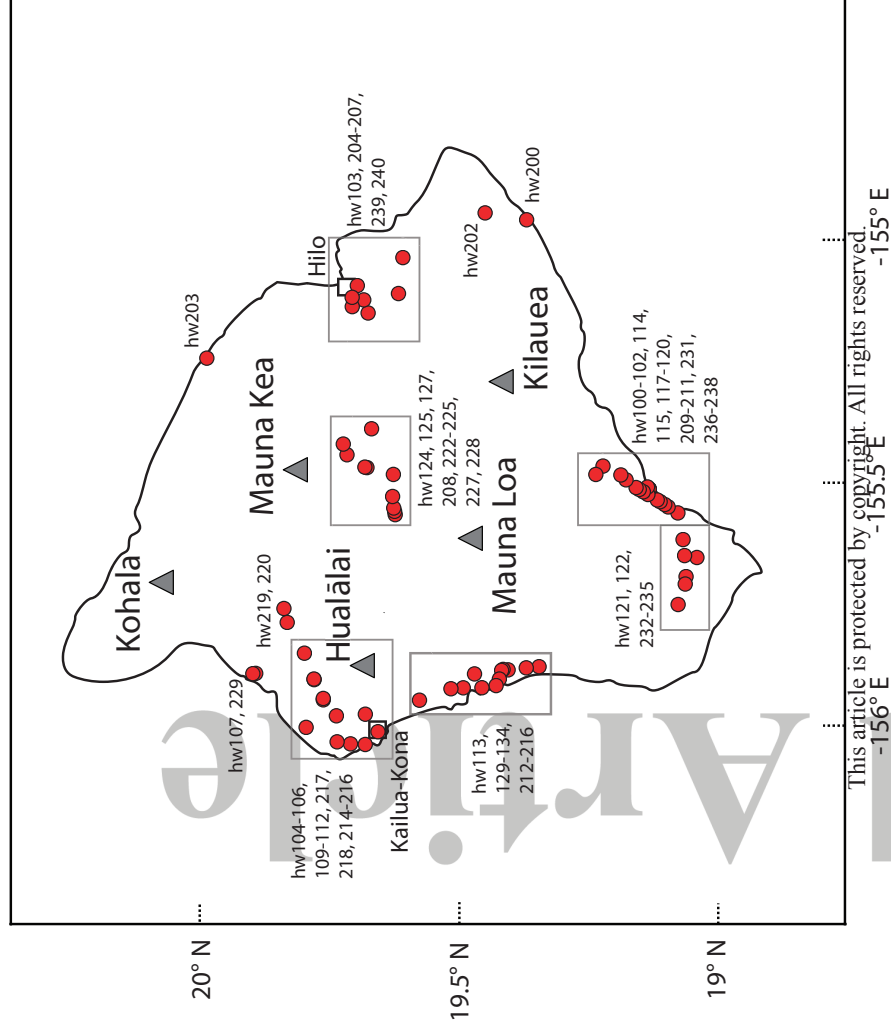


Figure 2.

Accepted Article



a)



b)



c)

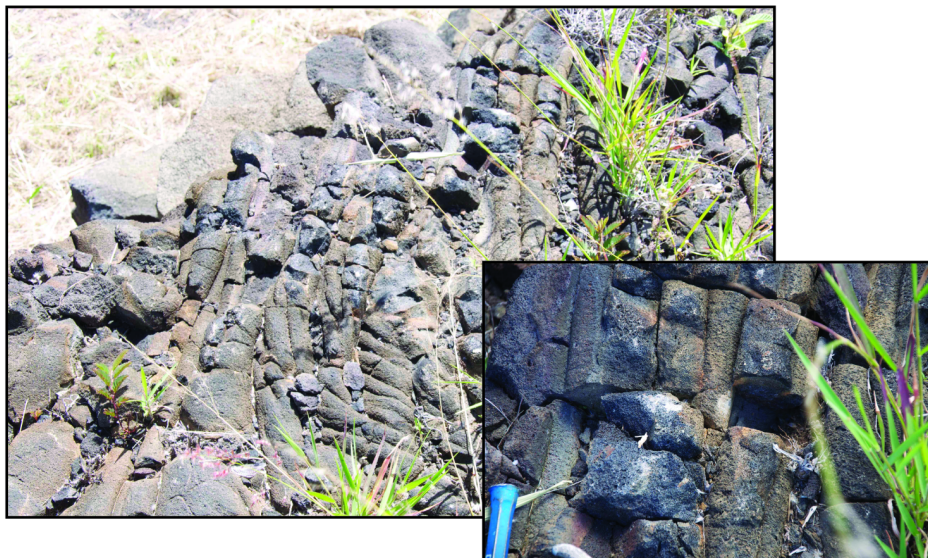
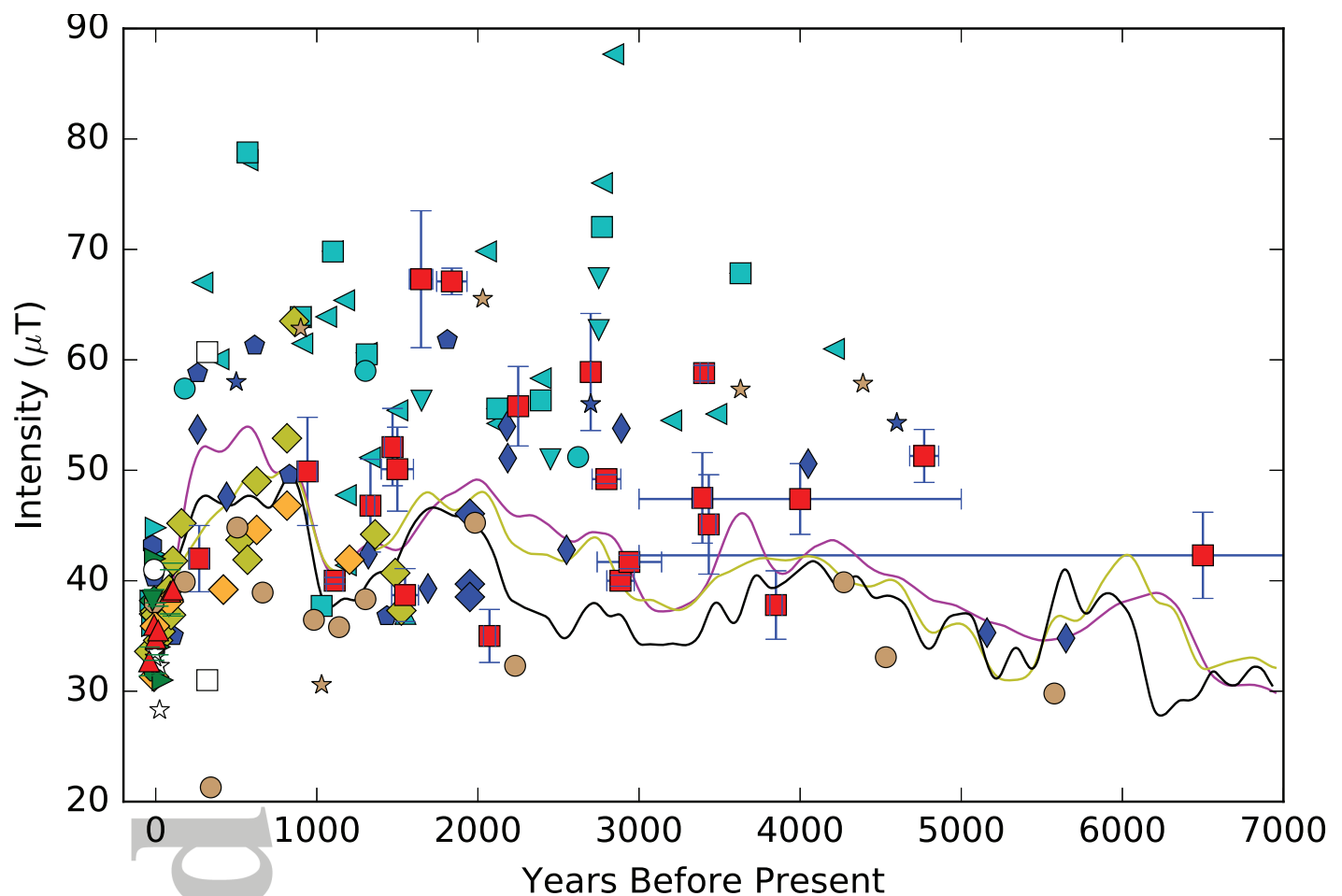


**Figure 3.**

Accepted Article





#### IZZI-Thellier

- This study
- ▲ Cromwell et al., 2015
- ◆ DeGroot et al., 2013

#### Thellier-Thellier

- ▶ Chauvin et al., 2005
- ▲ Laj and Kissel, 1999
- ▼ Laj et al., 2002
- ◀ Pressling et al., 2006
- Pressling et al., 2007
- Teanby et al., 2002

#### Aitken-Thellier

- ◁ Valet et al., 1998

#### Coe-Thellier

- ★ Coe et al., 1978
- Cottrell and Tarduno, 1999
- ◆ Mankinen and Champion, 1993
- Oishi et al., 2005
- ◆ Tanaka and Kono, 1991

#### Pseudo-Thellier

- ◆ DeGroot et al., 2013

#### Microwave

- Gratton et al., 2005
- Hill and Shaw, 2000
- ★ Pressling et al., 2007

#### MSP-DSC

- ◆ DeGroot et al., 2013

#### Shaw

- ▼ DeGroot et al., 2013
- ▶ Oishi et al., 2005
- ◀ Shaw, 1974

#### Other

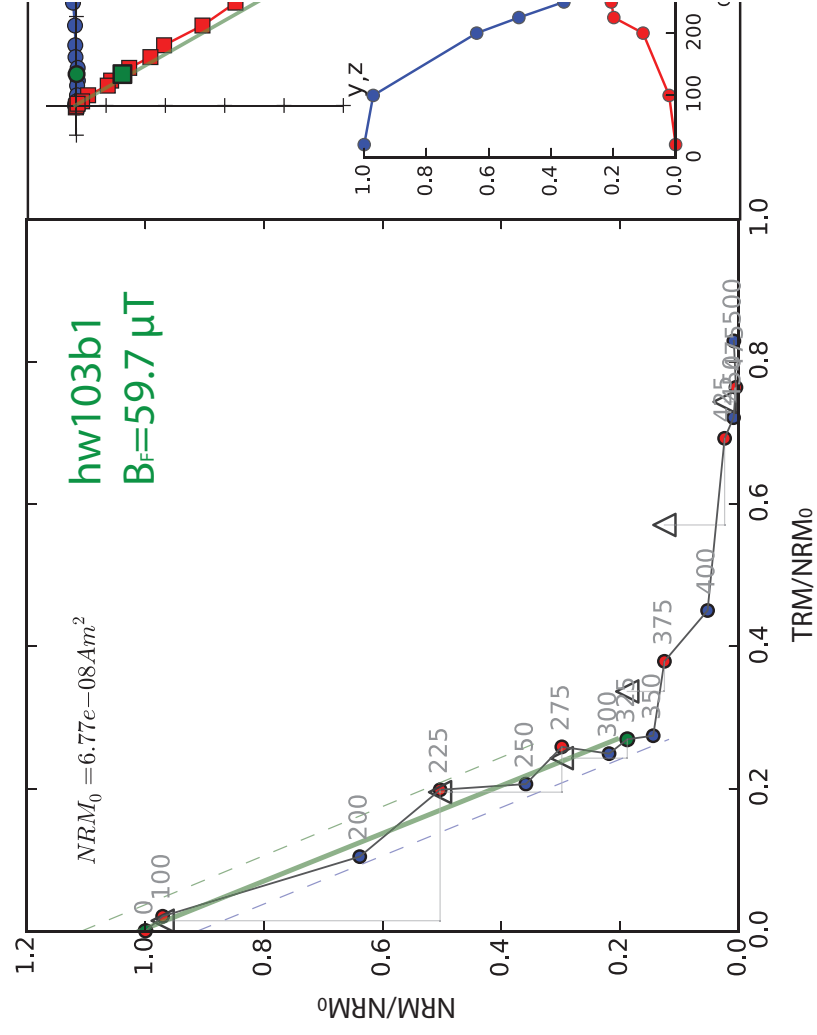
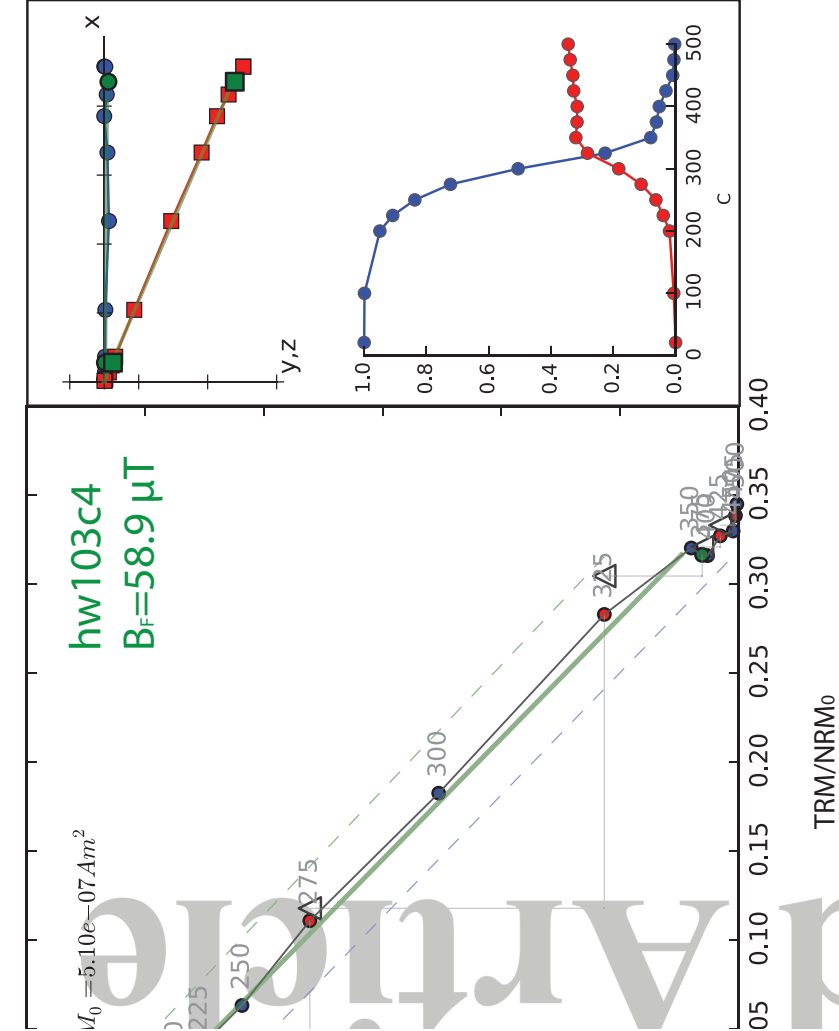
- Doell and Cox, 1972
- ★ Doell and Smith, 1969
- Tanaka et al., 1995

#### Paleointensity Models

- PFM9K
- CALS10K.2
- HFM.OL1.A1

Figure 4.

Accepted Article



d)

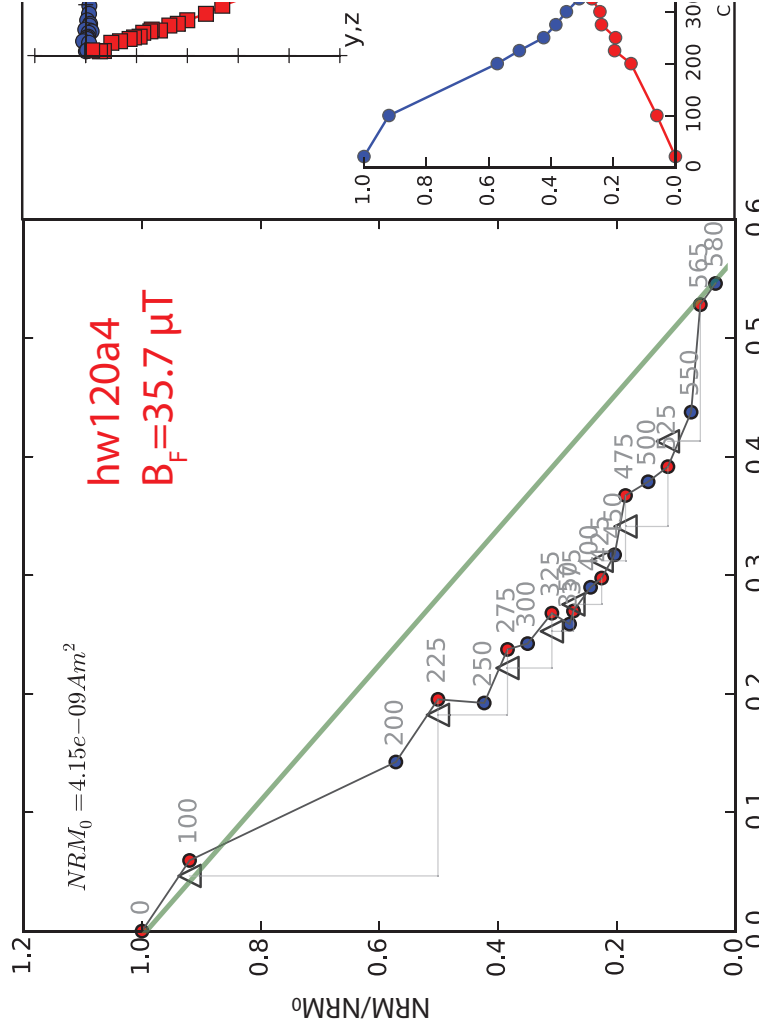
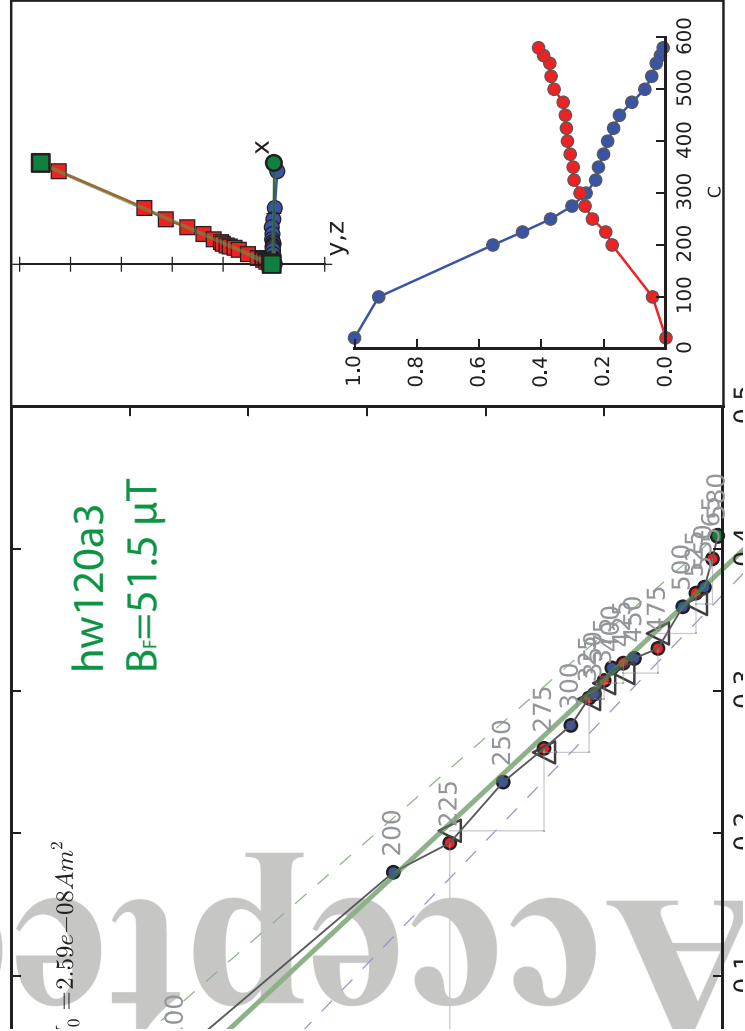


Figure 5.

Accepted Article

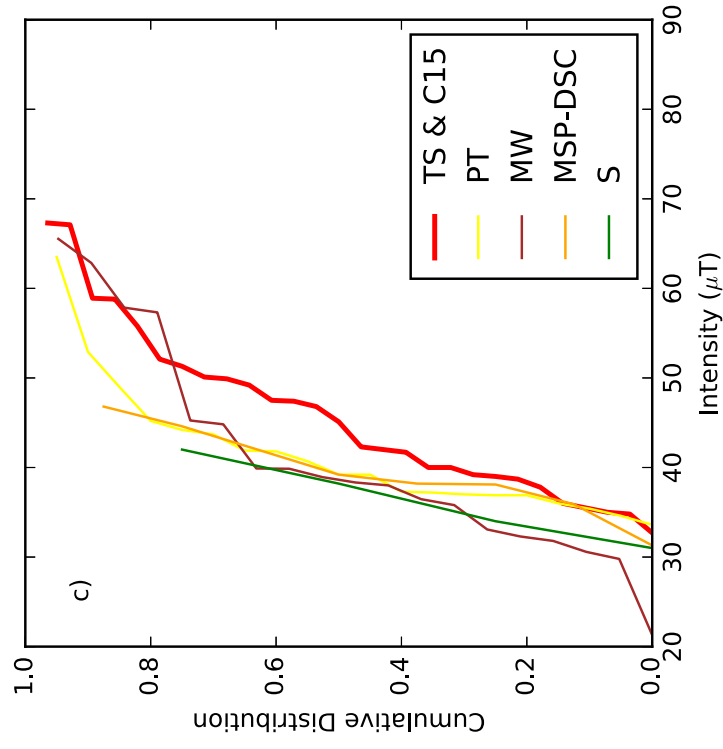
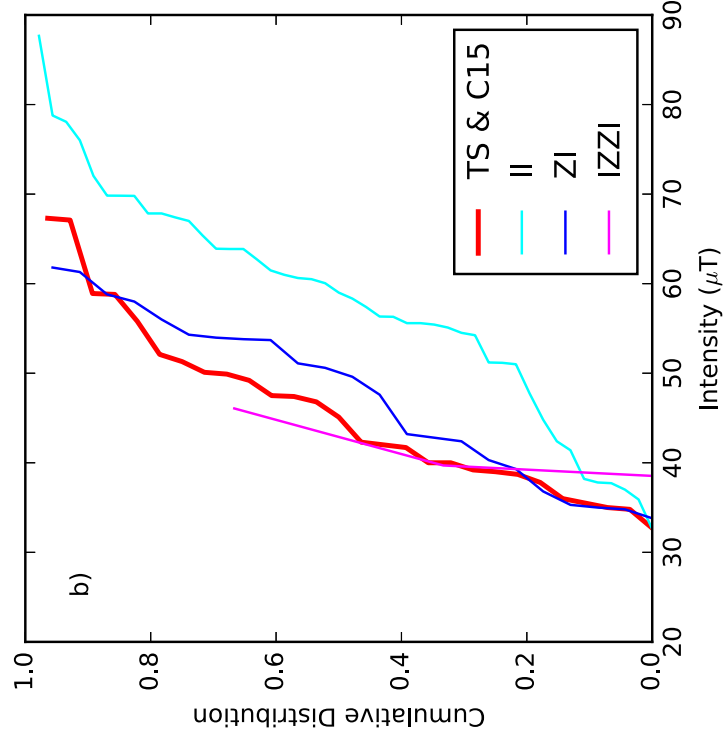
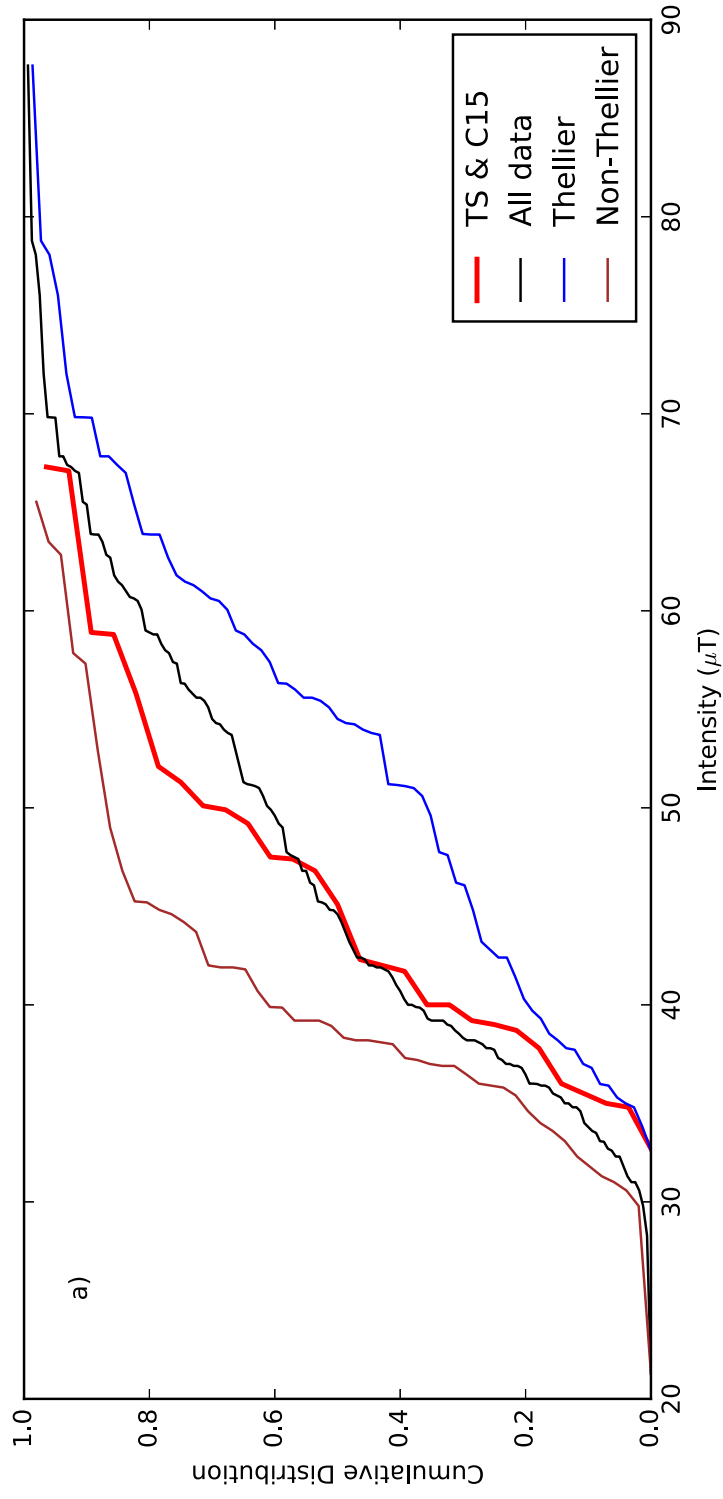
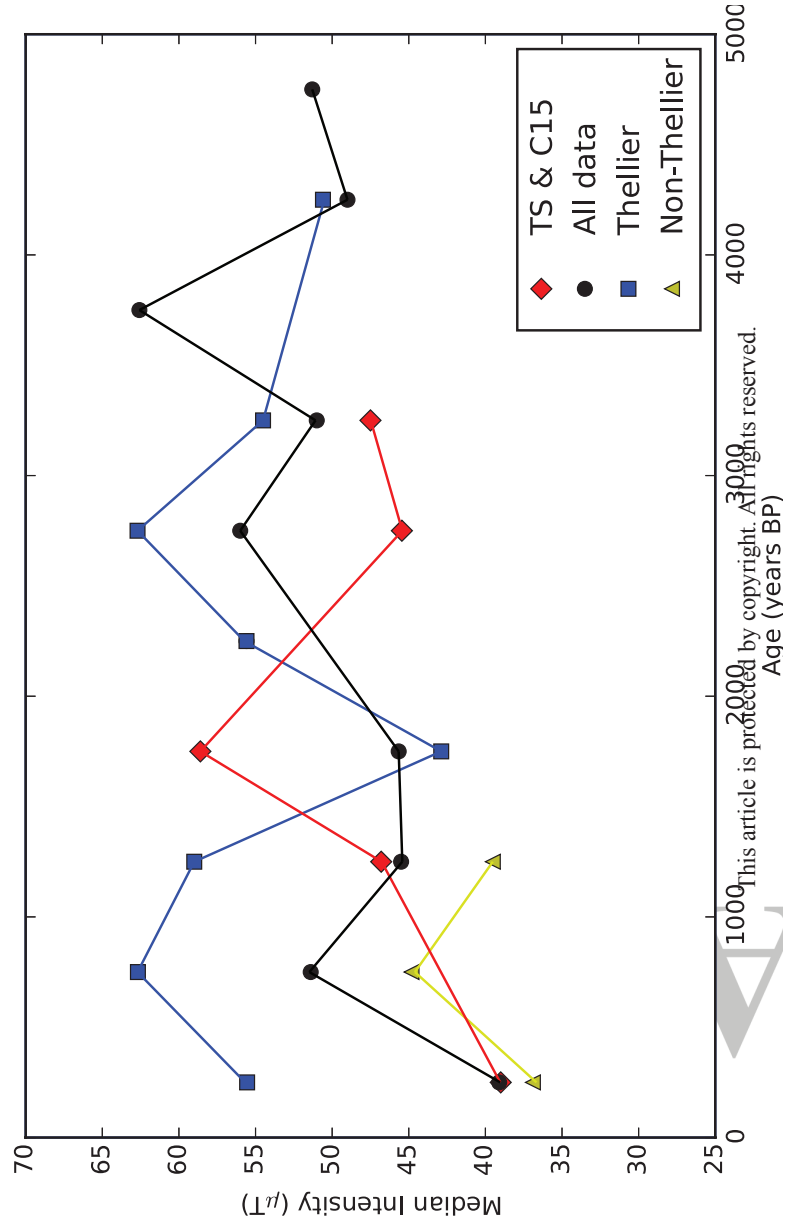


Figure 6.

Accepted Article



**Figure 7.**

Accepted Article



